Towards cluster state generation using charged quantum dot

Implementing small scale quantum algorithms in photonic cluster states

Master's Thesis

Written by *Rasmus Bruhn Nielsen*

22-05-2023

Supervised by

Peter Lodahl (lodahl@nbi.ku.dk)

Alexey Tiranov (alexey.tiranov@nbi.ku.dk)

University of Copenhagen

UNIVERSITY OF COPENHAGEN

FACULTY: Science

INSTITUTE: Niels Bohr Institute

AUTHOR(S): Rasmus Bruhn Nielsen

EMAIL: bzr977@alumni.ku.dk

TITLE AND SUBTITLE: Towards cluster state generation using charged quantum dot

- Implementing small scale quantum algorithms in photonic cluster states

Abstract

Quantum computers are receiving an increasing amount of attention from the public due to the promises of unlocking the ability to solve problems which, up until this point, has been unsolvable on classical computers. This includes applications in cryptography, physics, and the medical industry [26]. However, to get to the point of solving these problems a scalable, fault tolerant quantum computer must be developed. This requires, among other things, long lived qubits resistant to noise, efficient single qubit operations and efficient and scalable 2-qubit operations for realizing quantum entanglement between qubits. This thesis explores the possibility of using photon based qubits as a building block for a quantum computer. The system of a negatively charged InAs quantum dot embedded within a GaAs waveguide is presented along with an excitation scheme to generate highly indistinguishable time-bin encoded single photons entangled with the electron spin. A theoretical derivation of the optical spin control and photon generation protocol will be given while also discussing possible error sources and the significance of these. The spin-echo and nuclear spin narrowing sequences are also discussed as possible solutions to minimizing the decoherence of the spin. The experimental setup is described including the polarization and power control of the lasers used for spin control and photon generation, the temperature stabilization of the setup and the self stabilizing interferometer which is used in both the generation and measurement phase of the time-bin encoding. A simulation approach to speed up the optimization of PID parameters for PID's with a large input delay is also discussed. The main focus of this thesis is the generation protocol for GHZ states and linear cluster states using time-bin encoded photons and an implementation of Deutsch's algorithm in these. The theoretical background for measurement based quantum computations is described along with the implementation of Deutsch's algorithm used in the experimental work. A 3-qubit GHZ state was realized in the experiment with an extracted fidelity of $F = 0.56 \pm 0.02$. A three qubit version of Deutsch's algorithm was implemented in this state yielding the fidelity 0.88 ± 0.02 (0.85 ± 0.01) for the constant (balanced) version of the algorithm. Finally a Monte Carlo simulation was set up with realistic error parameters achieving a fidelity of 0.53. Simple improvements to the error parameters were added improving the fidelity to 0.66 suggesting a huge possible improvement to the fidelity. Using the improved parameter a 4-qubit linear cluster state was simulated to yield a fidelity of 0.48.

Preface

This thesis is the product of 9 months of research carried out in the Quantum Photonics group at the Niels Bohr Institute, University of Copenhagen under supervision of professor Peter Lodahl and Dr. Alexey Tiranov. I got the exciting opportunity to join the spin project which was started by Martin Hayhurst Appel back in 2016 and attempts to utilize a charged quantum dot to produce chains of entangled photons. This has allowed me to get to understand the challenges of working on a complex experimental setup and work with dedicated researchers to optimize, modify, and characterize the system.

First I would like to thank Peter Lodahl for giving me the opportunity to work on this exciting project, encourage me to take on this challenge and for his continued guidance. I would also like to thank Alexey Tiranov for teaching me the basics of working in a photonics lab and for his constant availability and assistance. Furthermore, I would like to express my gratitude to Yijian Meng and Ming Lai Chan for teaching me the ins and outs of the setup and for their continued support and help throughout the project. I would also like to thank Love Alexander Mandla Pettersson for our great discussions on quantum algorithms. I also want to give my gratitude to the rest of the Quantum Photonics group for all the scientific discussions, the great atmosphere and for helping me and giving me feedback throughout the past 9 months. Finally I want to thank my family and friends for being very supportive throughout my project and the rest of my studies.

Contents

1 Introduction

Since the development of quantum mechanics in the early 20th century we have attempted to further our understanding of the quantum world and how to control materials at a quantum level. One such attempt was the idea of a quantum computer [4, 14, 12] in which a 2-level system would be used as a quantum bit (qubit). The physics of superposition in qubits could in theory be used to make certain classically intractable problems tractable. Several quantum algorithms such as Shor's prime factorization algorithm [33] has been proposed. However, such algorithms requires large fault tolerant quantum computer. The choice in qubit is important since the different physical systems has different advantages and disadvantages. Many systems such as ions [28], superconductors [13], spins [31], and photons [19] has been explored as possible candidates for qubits and is being continuously investigated.

Photonic qubits are especially interesting since these can easily be transfered between distant locations and used for both quantum cryptography and quantum computing. Photonic qubits has been realized in various experiments [30, 18]. However, these results are non-deterministic and therefor difficult to scale up to full scale quantum computing. To solve this a lot of work has been done in deterministic single photon generation [36, 24, 6]. Using these deterministic sources, in principle, allows for scalable quantum computing using photons.

Deterministic generation of photons must be done with high efficiency and indistinguishability since low efficiency removes the advantage of being deterministic and indistinguishability is required for high fidelity operations. Single photon generation is usually done using an excitation and subsequent decay of some discrete energy structure. Many platforms exists for generating single photons including atoms or ions [3], organic molecules [32], defect centers [9], and semiconductors [16]. Each source has its own advantages and disadvantages in manufacturing, reliability, and performance.

Semiconductors has a lot of potential. Semiconductors support the growth of quantum dots which are defects in a bulk semiconductor made of another semiconductor with a different band gap. This is known as an "artificial atom" since the quantum well created by the localized defect can be used as an effective 2-level system. This has been achieved for a variety of different semiconductors [27, 20, 37].

This thesis focuses on the InAs quantum dots in GaAs. This is a platform which has been heavily investigated in recent years [5, 25, 29, 8, 17, 10, 7] due to the promising purity and indistinguishability of single photons generated by these [11]. This thesis will focus on generation of entangled photons using charged InAs quantum dots and the possibility of using these for quantum computing.

Chapter 2 will introduce the physical system used including the quantum dot and the photonic waveguide, along with the energy structure, selection rules, and noise sources. Chapter 3 will go through the theory of the spin control and photon generation protocol. Several possible sources of infidelity within these protocols will also be

investigated. Chapter 4 introduces the experimental setup used to generate the photons in the lab including the physical system, the lasers, and the interferometer used for time-bin encoding. Chapter 5 will go over the related topic of PID optimization and using simulations to speed up the process. Chapter 6 introduces the theory of measurement based quantum computing. The protocols for generating GHZ and linear cluster states are introduced and Deutsch's algorithm will be derived along with how to implement it in the experimental states. Chapter 7 works through the various error sources in the system and how to model them numerically, a Monte Carlo simulation is set up and used to break down the contributions of all the error sources to the state infidelity. Chapter 8 shows all of the experimental result and chapter 9 concludes the thesis and lists possible future work to improve the system.

2 The physical system

This chapter contains a simple description of the physical system. It will describe the physical structure of the chip, the optical selection rules for excitation, the photon collection system, and the error sources of the system and environment. This chapter is inspired by Martin Hayhurst Appel's PhD thesis [1] and is described in more detail there.

2.1 Quantum dot

In quantum optics an important experimental ability is to be able to produce highly indistinguishable single photons on demand. This can be achieved with a quantum emitter coupled to a single well defined optical mode. An excitation and subsequent decay of the emitter can produce a single photon and if the quantum emitter is well isolated from the environment, such that energy splitting is well defined and constant, these photons can be highly indistinguishable. Choosing a quantum emitter involves a lot of considerations. Among other things the emitter must be able to produce highly indistinguishable photons, operations on the emitter must be able to be done with high fidelity, and it needs high collection efficiency.

There are a lot of options but for this work a solid state quantum dot (QD) is used. By manufacturing a wafer of one material and replacing a small region of it with a different material with a smaller band gap, a quantum well can be created at the location of the defect introducing an effective 2-level system as shown in figure 1. This type of quantum emitter avoids the problem of having to trap the emitter which other systems, like atoms, has to deal with. It can also be integrated into a nanophotonic waveguide which can couple it to a single mode with a very high efficiency. This approach does have issues too. The main issue is that by nature of being a solid state system it is very well coupled to its environment. This can cause all sorts of issues and overcoming these is the main challenge of this system. Most of these issues are related to temperature and thus cooling it down inside a cryostat can help but will not fix everything.

2.1.1 Structure

In this work the emitter of choice is an indium arsenide (InAs) quantum dot embedded within a larger gallium arsenide (GaAs) wafer. The quantum dots are grown probabilistically by depositing single layers of InAs on a flat GaAs wafer [22]. Because InAs has a 7% larger lattice constant than GaAs [1] the InAs will spontaneously form domes as this is energetically favourable. These dome shaped quantum dots are typically around 20 nm wide and 5 nm tall [38]. InAs and GaAs are both semiconducters which has band structures of a valence band filled with electrons and a conduction band at higher energy which is empty and separated from the valence band by a bandgap. It is also important that this bandgap is a direct bandgap allowing it to produce photons. The bandgap of InAs is smaller than that of GaAs which results in the formation of a 3D quantum well at the position of the quantum dot. This quantum well allows for confined discrete electronic states in the otherwise continuous electronic states of the bands.

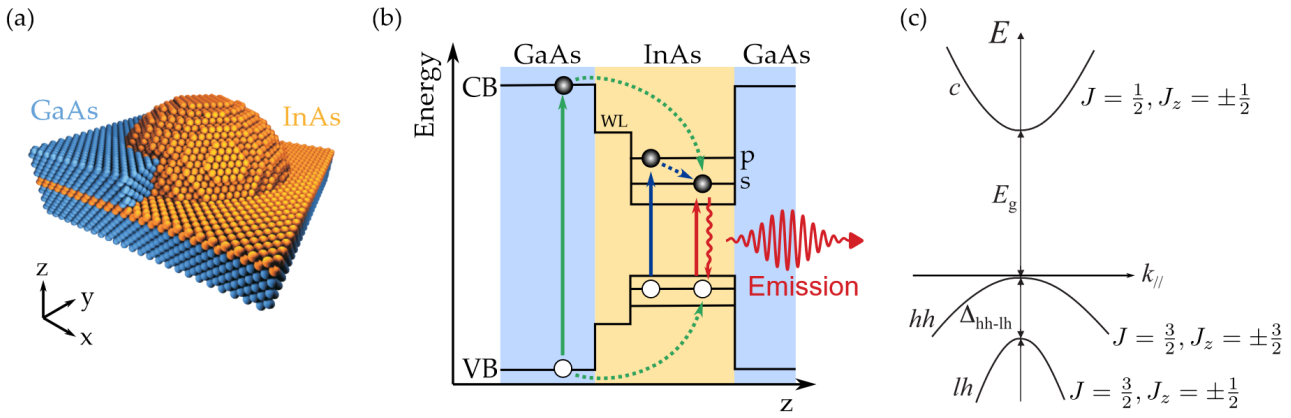

Figure 1: *(a) Illustration of a single quantum dot: The dome shaped InAs quantum dot is embedded with a larger GaAs structure.* ***(b)*** *Valence band (VB) and conduction bands (CB) energies inside the QD as a function of the vertical position. The smaller InAs bandgap produces a quantum well giving rise to quantized electronic states (horizontal lines).* ***(c)*** *The band diagram of the semiconducters used. The conduction band (top) and heavy hole valence band (hh) are separated by an energy splitting E_g and the hh band is separated from the light hole valence band (lh) by an energy splitting Δ_{hh-lh} due to strain. The figure is taken from Martin Hayhurst Appel's PhD thesis [1]*

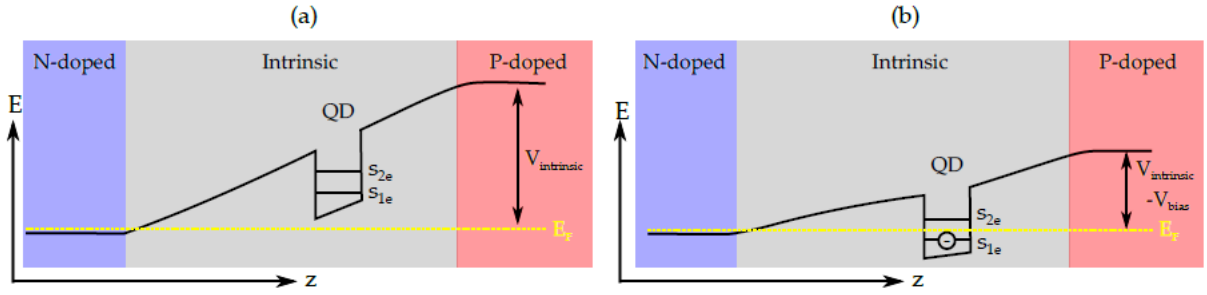

Figure 2: *Charging of a QD using a heterostructure. The energy along the z-direction changes due to an electric field generated by an applied voltage.* ***a)*** *The Fermi level is below the energy of the lowest electronic state leading to a neutral QD.* ***b)*** *The Fermi level is just high enough that the energy of a single electronic state is below it allowing for electrons to tunnel in and leading to a charged QD. The figure is taken from Martin Hayhurst Appel's PhD thesis [1]*

2.1.2 Charged state

The quantum dot can also be charged by adding an electron to the lowest energy level in the conduction band. This can be achieved by adding a bias voltage to the system allowing for electrons to tunnel into the quantum well as seen in figure 2. Once an electron is trapped in the well it is stable. This energy level has a s-like electronic structure [1] which has no angular momentum so the spin of the state is just given by the spin of the electron. By applying an external magnetic field in the xy-plane (Voight geometry) to the sample the energy of the spin states are split due to Zeeman splitting. This gives rise to a 4-state system given by the electron or trion (electron-exciton pair) with Zeeman splitting for each of them as seen in figure 3.

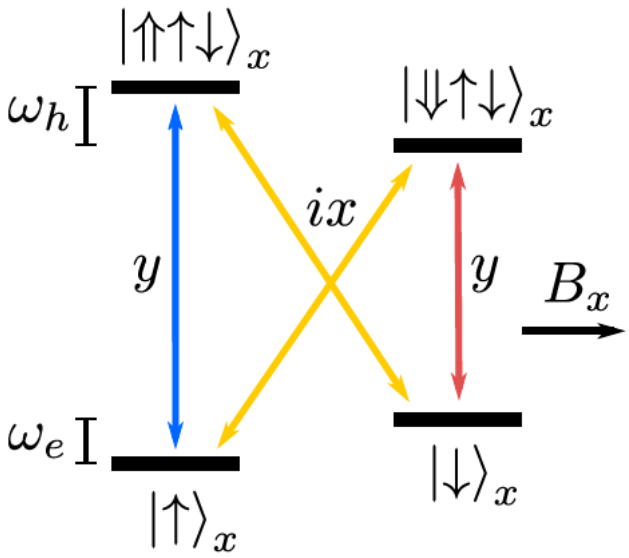

Figure 3: *The energy levels of the electron and negatively charged trion states. The electron state can be excited to a trion state either with a direct (y) transition or an indirect (ix) transition. These two transitions require opposite linear polarizations. The direction of the polarization is determined by the strain direction of the crystal. The figure is taken from Martin Hayhurst Appel's PhD thesis [1]*

2.1.3 Selection rules

To use the 4-state system the selection rules must be understood to be able to control the system. The electron can be excited to a negative trion state in two different ways. First a spin preserving excitation is possible using light of a specific linear polarization in the xy-plane, these are the direct (y) transitions. Second a spin flipping transition is possible using light polarized in the opposite linear direction in the xy-plane, these are known as indirect (ix) or diagonal transitions. The direction of the polarizations are determined by the strain direction of the crystal in which the QD is embedded. The energy structure and transitions are illustrated in figure 3. Typically, due to the photonic waveguide structure, the decay along either the direct or indirect transition is much more likely than the other. In this case the most likely decay transition is called the cycling transition and the other transition is the non-cycling transition. The cyclicity is defined as $C = \frac{\gamma}{\gamma'}$ where γ (γ') is the decay rate of the cycling (non-cycling) transition. Ideally the direct transition is the cycling transition since the energy splitting between the two direct transitions are greater than for the indirect transitions.

2.2 Photonic waveguide

The quantum dot by itself is able to generate single photons by the creation and subsequent decay of a trion state but the emission direction will be random. To solve this a photonic waveguide is created in the wafer. This is done by drilling holes in a hexagonal pattern in the wafer following the crystal lattice direction except for along a single line which will support a single optical mode. This is illustrated in figure 4. The quantum dot is then located within this waveguide. This allows for efficient collection of the generated photons and higher decay rate of the cycling transition due to Purcell enhancement. The probability for the QD to decay into the

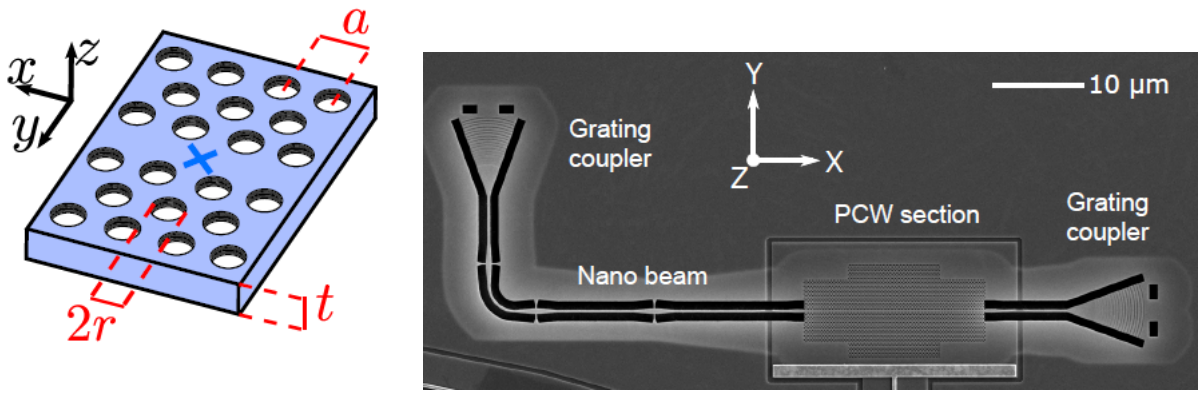

Figure 4: left) *An illustration of the waveguide structure in the wafer. The QD is located at the blue cross within the line of missing holes which functions as the waveguide.* ***right)*** *The full structure, the photonic crystal waveguide is connected with two grating couplers using nano beams. These grating couplers will couple the waveguide mode to a mode going out of the wafer. This is used to send laser into the waveguide or collect the photons created by the dot into fibers. The grating couplers have a right angle between them to couple to opposite polarizations to separate them more easily. The figure is taken from Martin Hayhurst Appel's PhD thesis [1]*

correct mode is given by $\beta = \frac{\gamma}{\gamma+\gamma'}$ where γ (γ') is the decay rate into the waveguide (environment). Beta factors of $\beta = 98.4\%$ has been achieved [2]. The orientation of the waveguide determines which of the two transitions will be Purcell enhanced and given the correct orientation cyclicities of $C = 30$ is possible.

Since the QD are created randomly they cannot be placed in the waveguide. This is solved by just making waveguides throughout the wafer and since there are a lot of QDs each waveguide is scanned and a waveguide with a good coupling to a quantum dot is chosen.

2.3 Noise sources

Since this is a solid state system it has a lot of noise sources which if not taken into account will kill any coherence in the system. Three sources of errors and how to minimize them will be discussed. These are phonon scattering, charge noise and the nuclear spin environment.

2.3.1 Phonons

There are two types of phonon scattering that can occur. The first is elastic phonon scattering. This is essentially small deformations of the structure due to vibrations. These deformations will slightly change the optical resonance frequency and occurs at a time scale of $100ps$ [34]. This can be modelled as a pure dephasing and will broaden the optical excitation energy spectrum. This will both have an effect during excitation of the system where it will lower the fidelity of the optical excitations and it will cause a lower indistinguishability of the generated photons.

The second type of scattering is inelastic phonon scattering where the QD may absorb or emit a phonon dur-

ing a decay. At low temperature the phonon occupation is low and thus phonon emission is more likely than absorption at cryogenic temperatures. This will cause a red detuned sideband in the emission spectrum which contain around $5 - 10\%$ of the photon emissions [23]. These photons are filtered out in the experiment and so this error can be modelled as a lower photon collection efficiency. Both of the phonon noise sources can be minimized by cooling the sample.

2.3.2 Charge noise

The second error source is charge noise. This arises from the electrostatic environment of the QD. This changes on the millisecond timescale [21] and will change the optical transition frequency due to the DC stark shift. Due to the slow timescale this does not affect the indistinguishability of the emitted photons but it will lower the fidelity of the optical excitations since every run of the experiment will have a different resonance frequency. This effect can be lowered by applying a voltage across the sample.

2.3.3 Nuclear spin environment

The last error source is due to the nuclear spin environment. Since the energy splitting of the electron spin states depends on the external magnetic field, it is also affected by coupling to the nuclear magnetic environment. The electron couples to $\sim 10^5$ atoms which all has spin and thus a small magnetic field. The electron interacts with them by the Fermi contact hyperfine interaction [21] and thus changes in the nuclear magnetic field will change the spin energy splitting. This leads to two different effects. The first is that a change in the magnetic environment leads to a random detuning of the spin rotation pulses just like charge noise does for the optical excitation. The second effect is since the Zeeman splitting of the spin states changes so does the speed of the spin precession. This effect leads to dephasing and is described by the T_2^* time. The low frequency component of the nuclear spin noise can be compensated using a spin-echo sequences which will rephase the spin. However, the random high frequency components cannot easily be corrected for and will cause dephasing errors. This effect can be minimized by doing nuclear spin narrowing where the nuclear spin ensemble is narrowed which lowers the fluctuations of the coupling field.

3 Photon generation and spin control

In this section the idea of photon generation and spin control is introduced. Spin initialization and detection will be discussed along with spin rotation through Raman pulses. Finally the photon generation protocol will be discussed and the spin-echo sequence will be explored.

3.1 Rabi oscillations

First the interaction between a 2-level system and a classical electromagnetic field is described. The 2-level system has the free Hamiltonian

$$\hat{H}^0 = -\frac{1}{2}\omega_0 \hat{\sigma}^z, \tag{1}$$

where ω_0 is the energy splitting and $\hat{\sigma}^z = |g\rangle\langle g| - |e\rangle\langle e|$ is the Pauli-z operator. The electric field at the position of the system (the wavelength is assumed to be much larger than the extent of the 2-level system) can be described by

$$\mathbf{E}(t) = \mathbf{E_0} f(t) \cos(\omega t), \tag{2}$$

where ω is the angular frequency of the field and $f(t)$ is an envelope function. For a monochromatic wave $f(t) = 1$. It is assumed that the 2-level system and the field interacts with a dipole interaction and the 2-level system is spherically symmetric. Then the interaction Hamiltonian is

$$\hat{H}^I(t) = -\hat{\mathbf{d}} \cdot \mathbf{E}(t) = -\hat{\mathbf{d}} \cdot \mathbf{E_0} f(t) \cos(\omega t) \equiv \hat{V} f(t) \cos(\omega t), \tag{3}$$

where the interaction strength is defined as $\hat{V} \equiv -\hat{\mathbf{d}} \cdot \mathbf{E_0}$. Since the 2-level system is spherically symmetric $\langle g|\hat{V}|g\rangle = \langle e|\hat{V}|e\rangle = 0$ since the dipole cannot have a preferred direction. To simplify the expression the definition $\hat{V} \equiv V\hat{\sigma}^x$ is used. It is assumed that V is real and $\hat{\sigma}^x = |g\rangle\langle e| + |e\rangle\langle g|$ is the Pauli-x operator. The free evolution of a state $|\psi\rangle \equiv |\psi(0)\rangle$ is

$$\begin{aligned} &\frac{\partial |\psi(t)\rangle}{\partial t} = -i\hat{H}^0 |\psi(t)\rangle \\ &|\psi(t)\rangle = \exp\left(-i\hat{H}^0 t\right) |\psi\rangle \equiv \hat{U} |\psi\rangle = \left(\exp(i\omega_0 t/2) |g\rangle\langle g| + \exp(-i\omega_0 t/2) |e\rangle\langle e|\right) |\psi\rangle . \end{aligned} \tag{4}$$

In a rotating frame with the definition $\left|\bar{\psi}(t)\right\rangle = \hat{U}^\dagger |\psi(t)\rangle$ the full Schrödinger equation becomes

$$\begin{aligned} &\frac{\partial \left|\bar{\psi}(t)\right\rangle}{\partial t} = \frac{\partial \hat{U}^\dagger}{\partial t} |\psi(t)\rangle + \hat{U}^\dagger \frac{\partial |\psi(t)\rangle}{\partial t} \\ &= i\hat{H}^0 \hat{U}^\dagger |\psi(t)\rangle - i\hat{U}^\dagger \left(\hat{H}^0 + \hat{H}^I\right) \hat{U}\hat{U}^\dagger |\psi(t)\rangle = -i\hat{\bar{H}} \left|\bar{\psi}(t)\right\rangle , \end{aligned} \tag{5}$$

with $\hat{\bar{H}} \equiv \hat{U}^\dagger \hat{H}^I \hat{U}$ being the Hamiltonian in the rotating frame. Now the bars are dropped and any operator will be asumed to be in the rotating frame. Then the Hamiltonian is

$$\hat{H} = \hat{U}^\dagger \hat{V} \hat{U} f(t) \cos(\omega t) = \frac{V}{2} f(t)(\exp(i\omega_0 t)\,|e\rangle\langle g| + \exp(-i\omega_0 t)\,|g\rangle\langle e|)(\exp(i\omega t) + \exp(-i\omega t)). \tag{6}$$

Next the rotating wave approximation (RWA) is used. In this approximation only the slowly varying terms are kept, then the final Hamiltonian is

$$\hat{H} = \frac{V}{2} f(t)(\exp(i\Delta t)\,|g\rangle\langle e| + \exp(-i\Delta t)\,|e\rangle\langle g|), \tag{7}$$

with $\Delta \equiv \omega - \omega_0$.

3.2 Decay mechanics

The mechanics of a 2-level system decaying and emitting a photon is described next. To do this a Monte Carlo approach is used. This derivation follows the derivation in section 8.3 of Introductory Quantum Optics [15]. The decay rate is defined as γ, the decay operator is defined to be $\hat{a}$ which can be a combination of fermionic/bosonic creation/annihilation operators. The probability for a decay to occur when in the state $|\psi\rangle$ in the time interval δt is

$$\Delta P = \gamma \delta t \,\langle \psi | \hat{a}^\dagger \hat{a} | \psi \rangle\,. \tag{8}$$

If the state decays the new state will be

$$|\psi_{emit}\rangle = \frac{\hat{a}\,|\psi\rangle}{\langle \psi | \hat{a}^\dagger \hat{a} | \psi \rangle^{1/2}} = \frac{(\gamma \delta t)^{1/2} \hat{a}\,|\psi\rangle}{\Delta P^{1/2}}. \tag{9}$$

If it does not decay it will be affected by the effective non-Hermitian Hamiltonian $\hat{H}_{eff} = \hat{H} - i\frac{\gamma}{2}\hat{a}^\dagger\hat{a}$. The idea behind this is that given no decay, then it is less likely to have been in the excited state. The resulting state will be

$$\begin{aligned} |\psi_{no-emit}\rangle &= \frac{\exp\left(-i\delta t \hat{H}_{eff}\right)|\psi\rangle}{\langle\psi|\exp\left(i\delta t \hat{H}_{eff}^\dagger\right)\exp\left(-i\delta t \hat{H}_{eff}\right)|\psi\rangle^{1/2}} \\ &\approx \frac{\left(1 - i\delta t \hat{H} - \frac{\gamma}{2}\delta t \hat{a}^\dagger\hat{a}\right)|\psi\rangle}{\langle\psi|1 - \gamma\delta t \hat{a}^\dagger\hat{a}|\psi\rangle^{1/2}} = \frac{\left(1 - i\delta t \hat{H} - \frac{\gamma}{2}\delta t \hat{a}^\dagger\hat{a}\right)|\psi\rangle}{(1-\Delta P)^{1/2}}. \end{aligned} \tag{10}$$

Now the pure state $|\psi\rangle\langle\psi|$ will evolve like ($|\psi\rangle \equiv |\psi(t)\rangle$)

$$\begin{aligned} &|\psi(t+\delta t)\rangle\langle\psi(t+\delta t)| = \Delta P\,|\psi_{emit}\rangle\langle\psi_{emit}| + (1-\Delta P)\,|\psi_{no-emit}\rangle\langle\psi_{no-emit}| \\ &= \gamma\delta t \hat{a}\,|\psi\rangle\langle\psi|\,\hat{a}^\dagger + \left(1 - i\delta t\hat{H} - \frac{\gamma}{2}\delta t\hat{a}^\dagger\hat{a}\right)|\psi\rangle\langle\psi|\left(1 + i\delta t\hat{H} - \frac{\gamma}{2}\delta t\hat{a}^\dagger\hat{a}\right) \\ &\approx |\psi\rangle\langle\psi| - i\delta t\Big[\hat{H}, |\psi\rangle\langle\psi|\Big] + \frac{\gamma}{2}\delta t\big(2\hat{a}\,|\psi\rangle\langle\psi|\,\hat{a}^\dagger - \hat{a}^\dagger\hat{a}\,|\psi\rangle\langle\psi| - |\psi\rangle\langle\psi|\,\hat{a}^\dagger\hat{a}\big). \end{aligned} \tag{11}$$

Taking the limit $\delta t \to 0$ and averaging over all the pure states to get the density matrix yields

$$\frac{\partial \hat{\rho}}{\partial t} = -i\Big[\hat{H}, \hat{\rho}\Big] + \frac{\gamma}{2}\big(2\hat{a}\hat{\rho}\hat{a}^\dagger - \hat{a}^\dagger\hat{a}\hat{\rho} - \hat{\rho}\hat{a}^\dagger\hat{a}\big), \tag{12}$$

which is the evolution of a density matrix with decay.

3.3 Spin initialization and detection

3.3.1 Initialization

In order to use the spin of the electron within the QD, the spin must first be initialized. The QD is assumed to be a 4-level system with the states $|0\rangle$, $|1\rangle$, $|2\rangle$ and $|3\rangle$. Cycling transitions are assumed to connect $|0\rangle$ to $|3\rangle$ and $|1\rangle$ to $|2\rangle$ and a non-cycling transition is assumed to connect $|0\rangle$ to $|2\rangle$ and $|1\rangle$ to $|3\rangle$. The state should be initialized to the $|0\rangle$ state. To do this the system will be excited with a laser resonant with the $|1\rangle \leftrightarrow |3\rangle$ non-cycling transition. At some point it will decay into the $|0\rangle$ state and will be unable to be excited any further. However, this is not the complete story since there is only a finite detuning to the $|0\rangle \leftrightarrow |2\rangle$ transition, thus this transition can also occur. The detuning between the two non-cycling transitions will be denoted by Δ. Then the Hamiltonian for the system is

$$\hat{H} = \frac{V}{2}(|1\rangle\langle 3| + |3\rangle\langle 1| + \exp(i\Delta t)\,|0\rangle\langle 2| + \exp(-i\Delta t)\,|2\rangle\langle 0|). \tag{13}$$

Then equation 12 becomes

$$\begin{aligned}
&\frac{\partial \rho}{\partial t} = -i\Big[\hat{H}, \rho\Big] \\
&+ \frac{\gamma}{2}(2(\rho_{22}(|1\rangle\langle 1| - |2\rangle\langle 2|) + \rho_{33}(|0\rangle\langle 0| - |3\rangle\langle 3|)) - (\rho_{12}\,|1\rangle\langle 2| + \rho_{21}\,|2\rangle\langle 1| + \rho_{03}\,|0\rangle\langle 3| + \rho_{30}\,|3\rangle\langle 0|)) \\
&+ \frac{\gamma'}{2}(2(\rho_{22}(|0\rangle\langle 0| - |2\rangle\langle 2|) + \rho_{33}(|1\rangle\langle 1| - |3\rangle\langle 3|)) - (\rho_{02}\,|0\rangle\langle 2| + \rho_{20}\,|2\rangle\langle 0| + \rho_{13}\,|1\rangle\langle 3| + \rho_{31}\,|3\rangle\langle 1|)).
\end{aligned} \tag{14}$$

Since only the $\hat{\rho}_{13}$ and $\hat{\rho}_{02}$ off diagonal states (and the opposite elements as well) can be pumped, the other off-diagonal elements will not be considered. The relevant equations are

$$\begin{aligned}
\frac{\partial \rho_{00}}{\partial t} &= -V\,\mathrm{Im}\{\exp(-i\Delta t)\rho_{02}\} + \gamma\rho_{33} + \gamma'\rho_{22} \\
\frac{\partial \rho_{11}}{\partial t} &= -V\,\mathrm{Im}\{\rho_{13}\} + \gamma\rho_{22} + \gamma'\rho_{33} \\
\frac{\partial \rho_{22}}{\partial t} &= V\,\mathrm{Im}\{\exp(-i\Delta t)\rho_{02}\} - (\gamma + \gamma')\rho_{22} \\
\frac{\partial \rho_{33}}{\partial t} &= V\,\mathrm{Im}\{\rho_{13}\} - (\gamma + \gamma')\rho_{33} \\
\frac{\partial \rho_{02}}{\partial t} &= -\frac{i}{2}V\exp(i\Delta t)(\rho_{22} - \rho_{00}) - \frac{\gamma'}{2}\rho_{02} \\
\frac{\partial \rho_{13}}{\partial t} &= -\frac{i}{2}V(\rho_{33} - \rho_{11}) - \frac{\gamma'}{2}\rho_{13}.
\end{aligned} \tag{15}$$

Defining $\rho_{02} \equiv i \exp(i\phi) \exp(i\Delta t) b$ and $\rho_{13} \equiv ia$ is used to simplify these equations. It can be seen that a must be real and b is defined to be real. Next the steady state solutions as time goes to infinity is considered. In this limit the diagonal of the density matrix, a and b are assumed to constants. Then the equations become

$$\begin{aligned}
0 &= -V\cos(\phi)b + \gamma\rho_{33} + \gamma'\rho_{22} \\
0 &= -Va + \gamma\rho_{22} + \gamma'\rho_{33} \\
0 &= V\cos(\phi)b - (\gamma+\gamma')\rho_{22} \\
0 &= Va - (\gamma+\gamma')\rho_{33} \\
0 &= V(\rho_{22} - \rho_{00}) + \Gamma\exp(i(\phi+\theta))b \\
0 &= V(\rho_{33} - \rho_{11}) + \gamma' a,
\end{aligned} \tag{16}$$

where $\gamma' + 2i\Delta \equiv \Gamma\exp(i\theta)$ where Γ is real. By adding line 2 and 4 together it is seen that $\rho_{22} = \rho_{33}$ and then line 3 and 4 becomes

$$\begin{aligned}
b &= \frac{\gamma+\gamma'}{V\cos(\phi)}\rho_{22} \\
a &= \frac{\gamma+\gamma'}{V}\rho_{22}.
\end{aligned} \tag{17}$$

Using these results line 5 and 6 becomes

$$\begin{aligned}
\rho_{00} &= \left(1 + \frac{\Gamma(\gamma+\gamma')\cos(\phi+\theta)}{V^2\cos(\phi)}\right)\rho_{22} \\
0 &= \frac{\Gamma(\gamma+\gamma')\sin(\phi+\theta)}{V^2\cos(\phi)}\rho_{22} \\
\rho_{11} &= \left(1 + \frac{\gamma'(\gamma+\gamma')}{V^2}\right)\rho_{22}.
\end{aligned} \tag{18}$$

From these $\phi = -\theta$ and $\cos(\theta) = \frac{\gamma'}{\Gamma}$, $\Gamma^2 = \gamma'^2 + 4\Delta^2$ can be shown. Finally this yields

$$\rho_{00} = \left(1 + \frac{\Gamma^2(\gamma+\gamma')}{\gamma V^2}\right)\rho_{22}. \tag{19}$$

Using the last condition that $1 = \rho_{00} + \rho_{11} + \rho_{22} + \rho_{33}$ the population in $|2\rangle$ is given as

$$\rho_{22} = \frac{1}{4 + \frac{\gamma'(\gamma+\gamma')}{V^2} + \frac{\Gamma^2(\gamma+\gamma')}{\gamma' V^2}} = \frac{V^2}{2(2V^2 + \gamma'(\gamma+\gamma')(1+2Q'_\Delta))}, \tag{20}$$

where $Q'_\Delta \equiv \left(\frac{\Delta}{\gamma'}\right)^2$ is the non-cycling quality factor, the cycling quality factor is defined as $Q_\Delta \equiv \left(\frac{\Delta}{\gamma}\right)^2$. After letting the system settle the driving field is terminated causing the populations in ρ_{22} and ρ_{33} to decay into the other populations. Since $\rho_{22} = \rho_{33}$ in total ρ_{00} and ρ_{11} will receive the same amount of decay meaning the final population in state $|1\rangle$ is $I \equiv \rho_{11} + \rho_{22}$ where I is also the infidelity of the initialization. The final form of I is

$$I = \frac{1}{2}\frac{2V^2 + \gamma'(\gamma+\gamma')}{2V^2 + \gamma'(\gamma+\gamma')(1+2Q'_\Delta)}. \tag{21}$$

Since the infidelity will increase with the power V^2, the lowest possible infidelity is given in the low power limit by

$$I_{min} = \frac{1}{2}\frac{1}{1+2Q'_\Delta}. \tag{22}$$

For realistic values of $\gamma' = 0.17$ GHz and $\Delta = 2\pi \cdot 10$ GHz the quality factor of $Q = 1.4 \cdot 10^5$ is found and the best infidelity is $I_{min} = 1.8 \cdot 10^{-6}$. But in reality the power has to be cranked up a bit since lower power will also mean longer initialization time and thus power errors and other spin flip mechanics are the main contributors to the infidelity.

3.3.2 Detection

The spin of the electron cannot directly be detected, instead photons must be generated conditioned on a specific spin state. This is done by repeating the experiment twice with a small variation. For the first experiment the state is prepared and the $|1\rangle \leftrightarrow |2\rangle$ transition is driven resonantly. This is repeated N times and any result where no photons where received is discarded. In the remaining results the state is known to have been in $|1\rangle$. For the second experiment the same state is prepared, then the spin is flipped and the same protocol is run. In the results kept here the state is known to have been $|0\rangle$. It is assumed that the driving is done for a short period of time thus only effects to first order in C^{-1} is kept. It is also assumed that the photon collection efficiency is ϵ. First it is considered what happens when the system is in the $|1\rangle$ state when the field is applied. In the perfect case a photon should be detected. The system is very similar to the initialization and thus the equations of motion are easily found to be

$$\begin{aligned}
\dot{\rho}_{11} &= -V\,\mathrm{Im}\{\rho_{12}\} + \gamma\rho_{22} \\
\dot{\rho}_{22} &= V\,\mathrm{Im}\{\rho\}_{12} - (\gamma+\gamma')\rho_{22} \\
\dot{\rho}_{12} &= \frac{-iV}{2}(\rho_{22}-\rho_{11}) - \frac{\gamma}{2}\rho_{12} \\
\dot{f}(t) &= \gamma'\rho_{22},
\end{aligned} \tag{23}$$

where $\rho_{00} + \rho_{33} \equiv f(t)$ and the transitions from the states $|0\rangle$ and $|3\rangle$ back to the $|1\rangle$ and $|2\rangle$ states are ignored since this is a second order process. Since $\gamma >> \gamma'$ it can be assumed that in the time the system reaches a steady state due to γ, the decay due to γ' is insignificant and thus for short time scales the equations of motion is

$$\begin{aligned}
\dot{\rho}_{11} &= -V\,\mathrm{Im}\{\rho_{12}\} + \gamma\rho_{22} \\
\dot{\rho}_{22} &= V\,\mathrm{Im}\{\rho_{12}\} - \gamma\rho_{22} \\
\dot{\rho}_{12} &= \frac{-iV}{2}(\rho_{22}-\rho_{11}) - \frac{\gamma}{2}\rho_{12}.
\end{aligned} \tag{24}$$

Defining $\rho_{12} \equiv ia$ and searching for steady state solutions yield

$$\begin{aligned} 0 &= Va - \gamma\rho_{22} \\ 0 &= V(\rho_{22} - \rho_{11}) + \gamma a. \end{aligned} \tag{25}$$

Combining these results in

$$\rho_{11} = \left(1 + \frac{\gamma^2}{V^2}\right)\rho_{22}, \tag{26}$$

with the total population of $\rho_{11} + \rho_{22} = 1 - f(t)$. This can be simplified to

$$\rho_{22} = \frac{V^2}{2V^2 + \gamma^2}(1 - f(t)). \tag{27}$$

Now the slower evolution of the states can be considered. Here the equation simplifies to

$$\dot{f}(t) = \frac{\gamma' V^2}{2V^2 + \gamma^2}(1 - f(t)) \equiv \Gamma_+(1 - f(t)). \tag{28}$$

Defining $g(t) \equiv 1 - f(t)$ the equation is $\dot{g}(t) = -\Gamma_+ g(t)$ with the solution

$$\begin{aligned} g(t) &= \exp(-\Gamma_+ t) \\ \rho_{22} &= \frac{\Gamma_+}{\gamma'}\exp(-\Gamma_+ t). \end{aligned} \tag{29}$$

If the field is applied for a duration of $\frac{\delta}{\Gamma_+}$ then the expected number of photons is

$$n_+ = \int_0^{\frac{\delta}{\Gamma_+}} dt\gamma\rho_{22} = C\Gamma_+ \int_0^{\frac{\delta}{\Gamma_+}} dt \exp(-\Gamma_+ t) = C(1 - \exp(-\delta)). \tag{30}$$

Given this, the probability of not detecting a photon (false negatives) is

$$F_n = 1 - (1 - \epsilon)^{n_+}. \tag{31}$$

Next the case of starting in the $|0\rangle$ state is checked out. In this case the equations of motion to first order in C^{-1} is

$$\begin{aligned} \dot{\rho}_{11} &= -V\,\mathrm{Im}\{\rho_{12}\} + \gamma\rho_{22} + \gamma'\rho_{33} \\ \dot{\rho}_{22} &= V\,\mathrm{Im}\{\rho_{12}\} - \gamma\rho_{22} \\ \dot{\rho}_{12} &= \frac{-iV}{2}(\rho_{22} - \rho_{11}) - \frac{\gamma}{2}\rho_{12} \\ \dot{\rho}_{00} &= -V\,\mathrm{Im}\{\exp(-i\Delta t)\rho_{03}\} + \gamma\rho_{33} \\ \dot{\rho}_{33} &= V\,\mathrm{Im}\{\exp(-i\Delta t)\rho_{03}\} - (\gamma + \gamma')\rho_{33} \\ \dot{\rho}_{03} &= \frac{-iV}{2}\exp(i\Delta t)(\rho_{33} - \rho_{00}) - \frac{\gamma}{2}\rho_{03}. \end{aligned} \tag{32}$$

Defining $\rho_{03} \equiv i \exp(i\Delta t) \exp(i\phi) b$ and $\rho_{12} \equiv ia$ yields the steady state equations

$$\begin{aligned} 0 &= Va - \gamma\rho_{22} \\ 0 &= V(\rho_{22} - \rho_{11}) + \gamma a \\ 0 &= V\cos(\phi)b - \gamma\rho_{33} \\ 0 &= V(\rho_{33} - \rho_{00}) + \Gamma \exp(i(\phi+\theta))b, \end{aligned} \tag{33}$$

where $\gamma + 2i\Delta \equiv \Gamma \exp(i\theta)$. From line 4 it can be seen that $\phi = -\theta$ and since $\tan(\theta) = \frac{2\Delta}{gamma}$ it can be shown that $\cos(\phi) = \frac{\gamma}{\Gamma}$. This leads to the equations

$$\begin{aligned} \rho_{11} &= \left(1 + \frac{\gamma^2}{V^2}\right)\rho_{22} \\ \rho_{00} &= \left(1 + \frac{\Gamma^2}{V^2}\right)\rho_{33}. \end{aligned} \tag{34}$$

Defining $\rho_{11} + \rho_{22} \equiv f(t)$ leads to

$$\begin{aligned} 1 - f(t) = \rho_{00} + \rho_{33} &= \left(2 + \frac{\Gamma^2}{V^2}\right)\rho_{33} \\ \rho_{33} &= \frac{V^2}{2V^2 + \Gamma^2}(1 - f(t)). \end{aligned} \tag{35}$$

Adding equation 32, line 1 and 2 and combining with this result yields

$$\dot{f}(t) = \frac{\gamma' V^2}{2V^2 + \Gamma^2}(1 - f(t)), \tag{36}$$

and defining $g(t) \equiv 1 - f(t)$ yields

$$\begin{aligned} \dot{g}(t) &= -\frac{\gamma' V^2}{2V^2 + \Gamma^2} g(t) \equiv -\Gamma_- g(t) \\ g(t) &= \exp(-\Gamma_- t). \end{aligned} \tag{37}$$

Finally the population is

$$\begin{aligned} f(t) = \rho_{11} + \rho_{22} &= \left(2 + \frac{\gamma^2}{V^2}\right)\rho_{22} \\ \rho_{22} &= \frac{V^2}{2V^2 + \gamma^2}(1 - \exp(-\Gamma_- t)) = \frac{\Gamma_+}{\gamma'}(1 - \exp(-\Gamma_- t)). \end{aligned} \tag{38}$$

The expected number of photons generated is

$$\begin{aligned} n_- &= \int_0^{\frac{\delta}{\Gamma_+}} dt \gamma \rho_{22} = C\Gamma_+ \int_0^{\frac{\delta}{\Gamma_+}} dt (1 - \exp(-\Gamma_- t)) \\ &= C\Gamma_+ \left(\frac{\delta}{\Gamma_+} - \frac{1 - \exp\left(-\delta\frac{\Gamma_-}{\Gamma_+}\right)}{\Gamma_-} \right) = C\delta - CQ'\left(1 - \exp\left(-\frac{\delta}{Q'}\right)\right) \approx \frac{C\delta^2}{2Q'}, \end{aligned} \tag{39}$$

where the approximation holds for $\frac{\delta}{Q'} << 1$ and $Q' \equiv \frac{\Gamma_+}{\Gamma_-} = \frac{2V^2+\Gamma^2}{2V^2+\gamma^2}$. In the low power limit it reduces to $Q' \approx 1 + 4\frac{\Delta^2}{\gamma^2} = 1 + 4Q_\Delta$. Finally the probability of detecting a photon (false positives) is

$$F_p = 1 - (1-\epsilon)^{n_-} \approx n_-\epsilon \approx \frac{C\epsilon\delta^2}{2Q'}. \tag{40}$$

For realistic values of $\gamma = 5$ GHz, $\Delta = 2\pi \cdot 10$ GHz, $C = 30$, $\epsilon = 0.01$ and $\delta = 1$ the result is $Q' = 633$, $F_n = 0.17$ and $F_p = 2.4 \cdot 10^{-4}$ and thus the detection error probability is $\frac{F_p}{F_n} = 0.0014$. However, in reality the false positives will be much higher due to background detections leading to a higher error probability.

3.4 Spin rotation

An important ability is to control the spin of the electron since this can be used to generate entanglement in the system. The two spin states of the system is separated by ≈ 20 GHz which is in the microwave regime. However, driving the transition with a normal microwave field is slow and a pi-pulse duration in the order of $5ns$ is required. Instead the rotation can be done with a Raman pulse, here an optically excited state is used as an intermediate step. The one problem with this is that the optically excited state will decay with rate γ which will cause decoherence, so to avoid this there must not be a large population in this state. First the system is defined. The model system has a ground ($|g\rangle$) and excited ($|e\rangle$) state separated by energy ω_0 and the optically excited auxiliary state ($|f\rangle$) separated from the excited state by energy ω_1. The system will now be driven with a field of frequency $\omega = \omega_1 - \Delta$ with amplitude modulated by $\cos\left(\frac{\omega_0 t+\phi}{2}\right)$ with equal coupling to the $|g\rangle \leftrightarrow |f\rangle$ and the $|e\rangle \leftrightarrow |f\rangle$ transitions. The Hamiltonian for the system is then

$$\hat{H} = \frac{a}{2}(\exp(i\Delta t)\,|e\rangle\langle f| + \exp(-i\Delta t)\,|f\rangle\langle e| + \exp(i(\Delta+\omega_0)t)\,|g\rangle\langle f| + \exp(-i(\Delta+\omega_0)t)\,|f\rangle\langle g|), \tag{41}$$

where $a = V\cos\left(\frac{\omega_0 t+\phi}{2}\right)$ where V is assumed to be real and V^2 is proportional to the power of the laser. A general state can be written as $|\psi\rangle = c_g\,|g\rangle + c_e\,|e\rangle + c_f\,|f\rangle$ and with the Schrödinger equation $\frac{\partial|\psi\rangle}{\partial t} = -i\hat{H}\,|\psi\rangle$ the equations of motion are

$$\begin{aligned}
\dot{c}_g &= \frac{-ia}{2}\exp(i(\Delta+\omega_0)t)c_f \\
\dot{c}_e &= \frac{-ia}{2}\exp(i\Delta t)c_f \\
\dot{c}_f &= \frac{-ia}{2}\exp(-i\Delta t)(c_e + \exp(-i\omega_0 t)c_g).
\end{aligned} \tag{42}$$

Next the definition $c_f \equiv \exp(-i\Delta t)\tilde{c}_f$ is used which leads to the new equations

$$\begin{aligned}
\dot{c}_g &= \frac{-ia}{2}\exp(i\omega_0 t)\tilde{c}_f \\
\dot{c}_e &= \frac{-ia}{2}\tilde{c}_f \\
\dot{\tilde{c}}_f &= \frac{-ia}{2}(c_e + \exp(-i\omega_0 t)c_g) + i\Delta\tilde{c}_f.
\end{aligned} \tag{43}$$

At this point it will be assumed that $\Delta >> \omega_0, \gamma, V$. This just means that the dynamics of the $i\Delta\tilde{c}_f$ term is much faster than any other dynamic and thus everything else can be assumed to be constant when considering this term. Assuming that $\tilde{c}_f = \tilde{c}_f^0 + \tilde{c}_f^1 \exp(i\Delta t)$ where $\tilde{c}_f^0$ and $\tilde{c}_f^1$ are assumed to be constant (change much slower than Δ^{-1}). Then from 43 line 3

$$\begin{aligned} i\Delta\tilde{c}_f^1 \exp(i\Delta t) = i\Delta\big(\tilde{c}_f - \tilde{c}_f^0\big) = \frac{-ia}{2}(c_e + \exp(-i\omega_0 t)c_g) + i\Delta\tilde{c}_f \\ \tilde{c}_f^0 = \frac{a}{2\Delta}(c_e + \exp(-i\omega_0 t)c_g). \end{aligned} \tag{44}$$

At this point the slower evolutions will be considered, for these $\exp(i\Delta t)$ is replaced with the average value which is 0. Therefor, the new equations are

$$\begin{aligned} \dot{c}_g = \frac{-ia}{2}\exp(i\omega_0 t)\tilde{c}_f^0 = \frac{-ia^2}{4\Delta}\exp(i\omega_0 t)(c_e + \exp(-i\omega_0 t)c_g) \\ \dot{c}_e = \frac{-ia}{2}\tilde{c}_f^0 = \frac{-ia^2}{4\Delta}(c_e + \exp(-i\omega_0 t)c_g). \end{aligned} \tag{45}$$

Rewriting $a^2 = V^2\cos^2\left(\frac{\omega_0 t+\phi}{2}\right) = \frac{V^2}{4}(2 + \exp(i(\omega_0 t + \phi)) + \exp(-i(\omega_0 t + \phi)))$ and assuming that $\omega_0 >> \Omega \equiv \frac{V^2}{8\Delta}$ allows to remove any term with $\exp(in\omega_0 t)$ for $n \neq 0$ leading to the new equations

$$\begin{aligned} \dot{c}_g = \frac{-i\Omega}{2}(2c_g + \exp(-i\phi)c_e) \\ \dot{c}_e = \frac{-i\Omega}{2}(2c_e + \exp(i\phi)c_g). \end{aligned} \tag{46}$$

Defining $c_e \equiv \exp(i\phi)\tilde{c}_e$ yields

$$\begin{aligned} \dot{c}_g = \frac{-i\Omega}{2}(2c_g + c_e) \\ \dot{c}_e = \frac{-i\Omega}{2}(2c_e + c_g). \end{aligned} \tag{47}$$

Combining these two equations yields the final differential equation

$$\ddot{c}_g + 2i\Omega\dot{c}_g - \frac{3}{4}\Omega^2 c_g = 0, \tag{48}$$

which can be solved using any method for solving linear constant coefficient ordinary differential equations. Using the characteristic equation approach leads to the equation $\lambda^2 + 2i\Omega\lambda - \frac{3}{4}\Omega^2 = 0$ with the solutions

$$\lambda_\pm = \frac{-2i\Omega \mp \sqrt{-4\Omega^2 + 3\Omega^2}}{2} = \frac{-i(2 \pm 1)}{2}\Omega, \tag{49}$$

yielding the solution

$$c_g = A\exp(-i\Omega t/2) + B\exp(-3i\Omega t/2). \tag{50}$$

With the initial conditions $c_g(0) = 1$ and $\dot{c}_g(0) = -i\Omega$

$$\begin{aligned} B &= 1 - A \\ A &= \frac{1}{2}. \end{aligned} \tag{51}$$

Combining these yields the final result

$$c_g = \exp(-i\Omega t)\cos(\Omega t/2). \tag{52}$$

Now c_e can be evaluated as

$$\exp(i\phi)\left(\frac{2i}{\Omega}\dot{c}_g - 2c_g\right) = \exp(-i\Omega t)\exp\left(i\left(\phi - \frac{\pi}{2}\right)\right)\sin(\Omega t/2), \tag{53}$$

And apart from a global phase the evolution of the state is

$$|\psi\rangle = \cos(\Omega t/2)\,|g\rangle + \exp\left(i\left(\phi - \frac{\pi}{2}\right)\right)\sin(\Omega t/2)\,|e\rangle\,, \tag{54}$$

which is just a resonant Rabi oscillation with Rabi frequency Ω around the ϕ-axis in the xy-plane.

Next the decay error will be discussed. The state $|f\rangle$ may decay in which case the spin will be randomized. If the decay rate is γ then the normalized decay rate (decay rate divided by Rabi frequency) is given by

$$\begin{aligned} &\tilde{\Gamma} \equiv \frac{1}{2\pi}\int_0^{\frac{2\pi}{\Omega}} dt\gamma|c_f|^2 \approx \frac{1}{2\pi}\int_0^{\frac{2\pi}{\Omega}} dt\gamma\left|\tilde{c}_f^0\right|^2 = \\ &\frac{\gamma V^2}{32\pi\Delta^2}\int_0^{\frac{2\pi}{\Omega}} dt|(\exp(i\omega_0 t)c_e + 2c_e + c_g + \exp(-i\omega_0 t)(c_e + 2c_g) + \exp(-2i\omega_0 t)c_g)|^2 \\ &\approx \frac{\gamma V^2}{32\pi\Delta^2}\int_0^{\frac{2\pi}{\Omega}} dt\left(|c_e|^2 + |2c_2 + c_g|^2 + |c_e + 2c_g|^2 + |c_g|^2\right) \\ &= \frac{\gamma V^2}{32\pi\Delta^2}\int_0^{\frac{2\pi}{\Omega}} dt\left(6 + 8\cos\left(\frac{\Omega t}{2}\right)\sin\left(\frac{\Omega t}{2}\right)\cos(\phi - \pi/2)\right) = \frac{3\gamma}{\Delta}. \end{aligned} \tag{55}$$

In reality there are two $|f\rangle$ states available but since these are very close in energy it is just as if there were a higher coupling to one state. Using realistic values of $\Delta = 2\pi \cdot 650$ GHz, $\gamma = 5$ GHz and $V^2 = 4.1 \cdot 10^4\ GHz^2$ a pi-pulse duration of $\frac{2\pi}{\Omega} = 5ns$ is achieved and a normalized decay rate of $\tilde{\Gamma} = 0.0037$ yielding a rotation quality factor of $Q \equiv \frac{1}{\tilde{\Gamma}} = 270$ which is the number of pi-pulses to apply before the Rabi amplitude has decayed to 1/e. In reality this quality factor is only around 30 which is due to another decoherence effect from the Rabi oscillations. The laser is somehow able to make incoherent spin flips of the electrons. This is possibly happening by kicking out the electron and allowing a new electron to tunnel in with a random spin. However, this is not yet completely understood.

3.5 Decoherence and Spin-Echo sequence

The effect of decoherence as described in section 2.3.3 can be modelled as a z-rotation on the spin with the phase

$$\chi = \int_0^T dt\Omega(t), \tag{56}$$

where $\Omega(t)$ is the phase accumulation per unit time and is defined by the evolution of the nuclear magnetic environment. This can be converted to the frequency domain by defining

$$\begin{aligned}
&\Omega(t) \equiv \int_{-\infty}^{\infty} d\omega\tilde{\Omega}(\omega)\exp\left(-i\omega t\right) \\
&\chi = \int_0^T dt \int_{-\infty}^{\infty} d\omega\tilde{\Omega}(\omega)\exp\left(-i\omega t\right) = 2\int_{-\infty}^{\infty} d\omega\frac{\tilde{\Omega}(\omega)}{\omega}\exp\left(-i\omega T/2\right)\sin\left(\omega T/2\right) \\
&\bar{\chi} \equiv \frac{\chi}{T}
\end{aligned} \tag{57}$$

If the nuclear enviroment evolves with a well defined frequency then

$$\begin{aligned}
\tilde{\Omega}(\omega) &= \frac{A}{2}(\exp\left(-i\phi\right)\delta(\omega-\omega_0) + \exp\left(i\phi\right)\delta(\omega+\omega_0)) \\
\bar{\chi} &= \frac{2A}{\omega_0 T}\sin\left(\omega_0 T/2\right)\cos\left(\omega_0 T/2+\phi\right).
\end{aligned} \tag{58}$$

Depending on the amplitude of this oscillation this effect can be detrimental if not considered. One solution is to choose T such that $\omega_0 T/2 = m\pi$ for m being an integer in which case this dephasing effect will disappear. However, if the nuclear environment is not a harmonic but still fluctuating with roughly the same frequency then there will be frequency components of $\omega_0 + \delta\omega$ where $\frac{\delta\omega}{\omega_0} << 1$. In this case to first order in the error the dephasing will be

$$\begin{aligned}
\bar{\chi} &= \frac{A}{m\pi}\frac{1}{1+\frac{\delta\omega}{\omega_0}}\sin\left(m\pi\left(1+\frac{\delta\omega}{\omega_0}\right)\right)\cos\left(m\pi\left(1+\frac{\delta\omega}{\omega_0}\right)+\phi\right) \\
&= \frac{A}{m\pi}\frac{1}{1+\frac{\delta\omega}{\omega_0}}\sin\left(m\pi\frac{\delta\omega}{\omega_0}\right)\cos\left(m\pi\frac{\delta\omega}{\omega_0}+\phi\right) \approx A\cos\left(\phi\right)\frac{\delta\omega}{\omega_0}.
\end{aligned} \tag{59}$$

From this result it is clear that it will still decohere to first order in $\frac{\delta\omega}{\omega_0}$. However, there will most likely also be a constant component in which case

$$\bar{\chi} = \tilde{\Omega}(0), \tag{60}$$

which cannot be correct for if $\tilde{\Omega}(0)$ is not known. A solution to this is to implement a spin-echo pulse sequence. In this sequence the system will freely evolve for a time τ, then a pi-rotation is applied. After this rotation the dephasing will switch sign allowing the system to rephase until a time τ after the rotation when the constant component has completely rephased. This sequence is then repeated N times for a total sequence length of $2N\tau$. In this case

$$
\begin{aligned}
\chi &= \int_0^{\tau} dt\Omega(t) + \sum_{n=1}^{N-1} (-1)^n \int_{(2n-1)\tau}^{(2n+1)\tau} dt\Omega(t) + (-1)^N \int_{(2N-1)\tau}^{2N\tau} dt\Omega(t) \\
&= 2\int_{-\infty}^{\infty} d\omega \frac{\tilde{\Omega}(\omega)}{\omega} [\exp(-iN\omega\tau)\left(\exp\left(i\left(N-\frac{1}{2}\right)\omega\tau\right) + (-1)^N \exp\left(-i\left(N-\frac{1}{2}\right)\omega\tau\right)\right)\sin(\omega\tau/2) \\
&+ \sin(\omega\tau)\sum_{n=1}^{N-1}(-1)^n \exp(-2in\omega\tau)] \\
\bar{\chi} &= \frac{\chi}{2N\tau}.
\end{aligned}
\tag{61}
$$

This equation is significantly different for even and odd N.

$$
\begin{aligned}
\bar{\chi}_N &= \frac{A}{N\omega_0\tau}\left[2\cos(N\omega_0\tau+\phi)\cos\left(\left(N-\frac{1}{2}\right)\omega_0\tau\right)\sin(\omega_0\tau/2) + \sin(\omega_0\tau)\sum_{n=1}^{N-1}(-1)^n\cos(2n\omega_0\tau+\phi)\right] \\
\bar{\chi}_N &= \frac{A}{N\omega_0\tau}\left[2\sin(N\omega_0\tau+\phi)\sin\left(\left(N-\frac{1}{2}\right)\omega_0\tau\right)\sin(\omega_0\tau/2) + \sin(\omega_0\tau)\sum_{n=1}^{N-1}(-1)^n\cos(2n\omega_0\tau+\phi)\right],
\end{aligned}
\tag{62}
$$

for the even and odd cases respectively. From these results it is also clear that $\omega_0\tau = 2m\pi$ for m being an integer must be chosen to remove the error. Frequencies at $k\omega_0 + \delta\omega$ for k being an integer are studied. For N being even the following results are used

$$
\begin{aligned}
&\sum_{n=1}^{N-1}(-1)^n = -1 \\
&\sum_{n=1}^{N-1}(-1)^n n = -\frac{N}{2} \\
&\sum_{n=1}^{N-1}(-1)^n n^2 = -\frac{N(N-1)}{2},
\end{aligned}
\tag{63}
$$

and for N being odd

$$
\begin{aligned}
&\sum_{n=1}^{N-1}(-1)^n = 0 \\
&\sum_{n=1}^{N-1}(-1)^n n = \frac{N-1}{2} \\
&\sum_{n=1}^{N-1}(-1)^n n^2 = \frac{N(N-1)}{2}.
\end{aligned}
\tag{64}
$$

To lowest non-zero order in the expansion of the contents of the square brackets are

$$
\begin{aligned}
\bar{\chi}_N &= \frac{A}{k+\frac{\delta\omega}{\omega_0}} \cdot 2m^2\pi^2\cos(\phi)\left(\frac{\delta\omega}{\omega_0}\right)^3 \\
\bar{\chi}_N &= \frac{A}{k+\frac{\delta\omega}{\omega_0}} \cdot m\pi\sin(\phi)\left(\frac{\delta\omega}{\omega_0}\right)^2.
\end{aligned}
\tag{65}
$$

For k being non-zero the dephasing will be

$$\begin{aligned}\bar{\chi}_N &= \frac{A}{k}\cdot 2m^2\pi^2\cos(\phi)\left(\frac{\delta\omega}{\omega_0}\right)^3 \\ \bar{\chi}_N &= \frac{A}{k}\cdot m\pi\sin(\phi)\left(\frac{\delta\omega}{\omega_0}\right)^2.\end{aligned} \tag{66}$$

From this result it is seen that the spin-echo sequence corrects for the first and second order errors in $\frac{\delta\omega}{\omega_0}$ if an even number of pi-rotations are used or just first order if an odd number of pi-rotations are used. The error will also increase when m increases. From this result the best spin-echo sequence is one with an even number of pi-pulses and τ chosen such that $\omega_0\tau = 2\pi$. Apart from the parity of the number of pi-pulses the error is unaffected by the number of pi-pulses to lowest order in the error. The issue before was the low frequency noise. For $k = 0$ the dephasing is

$$\begin{aligned}\bar{\chi}_N &= 2Am^2\pi^2\cos(\phi)\left(\frac{\delta\omega}{\omega_0}\right)^2 \\ \bar{\chi}_N &= Am\pi\sin(\phi)\frac{\delta\omega}{\omega_0}.\end{aligned} \tag{67}$$

This result shows that the spin-echo sequence does correct for low frequency noise and everything is the same as for the higher frequency noise except the correction is done to a lower order. Thus the low frequency noise will affect the system more than harmonic noise.

3.6 Nuclear spin narrowing

Implementing a spin-echo sequence lowers the decoherence due to low frequency and harmonic noise in the nuclear spin environment. However the random noise is still a problem. To solve this a nuclear spin narrowing protocol can be implemented. The idea is to narrow the nuclear spin ensemble such that the fluctuations in the environment is lowered. This is achieved by exploiting the coupling between the electron spin and the nuclear spin environment. The Zeeman splitting of the electron spin increases with the number of excitations in the nuclear spins. Assume a Rabi oscillation is applied resonant to the system when the nuclear spins have N excitations. Also assume that the system has n excitations and the electron spin is in the spin up state $|\uparrow n\rangle$. Then the spin state can be rotated into one of three possible states $|\downarrow, n-1\rangle$, $|\downarrow, n\rangle$ and $|\downarrow, n+1\rangle$ with detunings Δ_{n-1}, Δ_n and Δ_{n+1}. The decoherence Δ_n will increase as $|N-n|$ increases which causes rotations towards the state with N excitations to be faster. This means that the system has a self stabilizing effect where the system will tend to minimize the detuning of the Rabi oscillation. This also means that the nuclear spin ensemble will narrow towards the state with N excitations just by performing a Rabi oscillation. Finally this effect can be speed up by coherently driving the non-cycling transition from the $|\downarrow\rangle$ state which is the same as in the initialization scheme.

To see how this works assume that the cycling decay rate is much faster than the Rabi oscillation. Now set up a model system with the 2 states $|0\rangle$ and $|e\rangle$ connected with the Rabi oscillation of power V^2 and detuning Δ.

The state $|e\rangle$ can decay into the last state $|1\rangle$ with decay rate γ. The Hamiltonian is

$$\hat{H} = \frac{V}{2}(\exp(i\Delta t)\,|0\rangle\langle e| + \exp(-i\Delta t)\,|e\rangle\langle 0|). \tag{68}$$

From equation 12 the equations of motion are found to be

$$\begin{aligned}
\dot{\rho}_{00} &= -V\,\mathrm{Im}\{\exp(-i\Delta t)\rho_{0e}\} \\
\dot{\rho}_{ee} &= V\,\mathrm{Im}\{\exp(-i\Delta t)\rho_{0e}\} - \gamma\rho_{ee} \\
\dot{\rho}_{0e} &= -\frac{iV}{2}\exp(i\Delta t)(\rho_{ee} - \rho 00) - \frac{\gamma}{2}\rho_{0e} \\
\dot{\rho}_{11} &= \gamma\rho_{ee},
\end{aligned} \tag{69}$$

and the decay rate into state $|1\rangle$ is then given by $\dot{\rho}_{11}$ when all the initial population is in state $|0\rangle$. Defining $\rho_{0e} \equiv i\exp(i\Delta t)a$ the new equation of motion for this term is

$$\dot{a} = -\frac{V}{2}(\rho_{ee} - \rho 00) - \frac{\Gamma\exp(i\theta)}{2}a, \tag{70}$$

where $\gamma + 2i\Delta \equiv \Gamma\exp(i\theta)$ where Γ is defined to be real and non-negative. Since $\gamma >> V$ then a will be at a constant steady state thus

$$a = -\frac{V}{\Gamma}(\rho_{ee} - \rho_{00})\exp(-i\theta). \tag{71}$$

Using this result the following is found

$$\begin{aligned}
&\mathrm{Im}\{\exp(-i\Delta t)\rho_{0e}\} = \mathrm{Re}\{a\} = -\frac{V}{\Gamma}(\rho_{ee} - \rho_{00})\cos(\theta) = -\frac{V\gamma}{\Gamma^2}(\rho_{ee} - \rho_{00}) \\
&\dot{\rho}_{00} = \frac{V\gamma}{\Gamma^2}(\rho_{ee} - \rho_{00}) \\
&\dot{\rho}_{ee} = -\frac{V\gamma}{\Gamma^2}(\rho_{ee} - \rho_{00}) - \gamma\rho_{ee}.
\end{aligned} \tag{72}$$

Again ρ_{ee} will also be at a steady state yielding

$$\begin{aligned}
\rho_{00} &= \left(1 + \frac{\Gamma^2}{V^2}\right)\rho_{ee} \\
\rho_{00} + \rho_{ee} &= 1 - \rho_{11} = \left(2 + \frac{\Gamma^2}{V^2}\right)\rho_{ee}.
\end{aligned} \tag{73}$$

Finally all of this can be combined into

$$\dot{\rho}_{11} = \gamma\rho_{ee} = \frac{V^2\gamma}{2V^2 + \Gamma^2}(1 - \rho_{11}). \tag{74}$$

Thus at the initial time $\rho_{11} = 0$ and the decay rate is

$$\gamma_\Delta = \frac{V^2\gamma}{2V^2+\Gamma^2} = \frac{V^2\gamma}{2V^2+\gamma^2+4\Delta^2} \approx \frac{V^2\gamma}{2V^2+\gamma^2}\left(1-\frac{4\Delta^2}{2V^2+\gamma^2}\right), \tag{75}$$

and thus the decay rate decreases as the detuning increases leading to a narrowing of the nuclear spin ensemble. It is also evident that lower power and lower decay rate will increase this effect, however, this will also decrease the speed of the narrowing allowing other broadening sources to be more dominant. This is also only a simple model for the system and does not convey the full story but it shows the principle of the narrowing.

3.7 Photon generation

Another core operation of the experimental system is the ability to coherently generate single photons on demand and conditioned on the spin state of the trapped electron. This can be achieved by applying a short laser pulse resonant with a cycling transition. If the correct power is applied a trion state will be created and subsequently decay back to the same spin state with a high probability while generating a single photon. To avoid double excitations which would kill the coherence the pulse duration must be much smaller than the lifetime of the trion state. The bandwidth of the laser pulse must also be much smaller than the detuning between the two cycling transitions. If this is not done the dot may be excited when it is in the wrong spin state. The generated photon would have a wrong frequency and would be filtered away but it is an effective measurement of the system collapsing any superposition of the spin state causing decoherence.

The pulse shape will be modelled as being Gaussian since it is simple and it has no large frequency components far from the central frequency. The dynamics of the system is just a Rabi oscillation which means the Hamiltonian is taken from equation 7

$$\begin{aligned}\hat{H} &= \frac{V}{2}f(t)(|1\rangle\langle 2| + |2\rangle\langle 1| + \exp(i\Delta t)\,|0\rangle\langle 3| + \exp(-i\Delta t)\,|3\rangle\langle 0|)\\ f(t) &= \frac{1}{\tau\sqrt{4\pi}}\exp\left(-\frac{t^2}{4\tau^2}\right),\end{aligned} \tag{76}$$

where τ is the characteristic time for the pulse related to the full width half maximum of the power profile by $FWHM = 2\sqrt{2\ln(2)}\tau$ and time is defined to be 0 when the pulse is maximum. It is assumed that the $|1\rangle \leftrightarrow |2\rangle$ transition is driven resonantly detuned by Δ compared to the $|0\rangle \leftrightarrow |3\rangle$ transition. On top of this the decay rate through the cycling transition is γ. This problem cannot be solved analytically so must be solved numerically. The system is simulated in figure 5. Only one of the transitions are simulated but since the coupling to both transitions are equal the different transitions are simulated by changing the detuning.

In the setup there is a 10 GHz detuning between the two cycling transitions. It is supposed to be 30 GHz but an error during manufacturing caused the indirect transitions to become the cycling transition. This in turn decreased the detuning. From the simulation it is clear that this has a huge effect. For 10 GHz detuning the probability to produce a wrong photon is up to 0.25 and the pulse cannot get any wider since the probability for

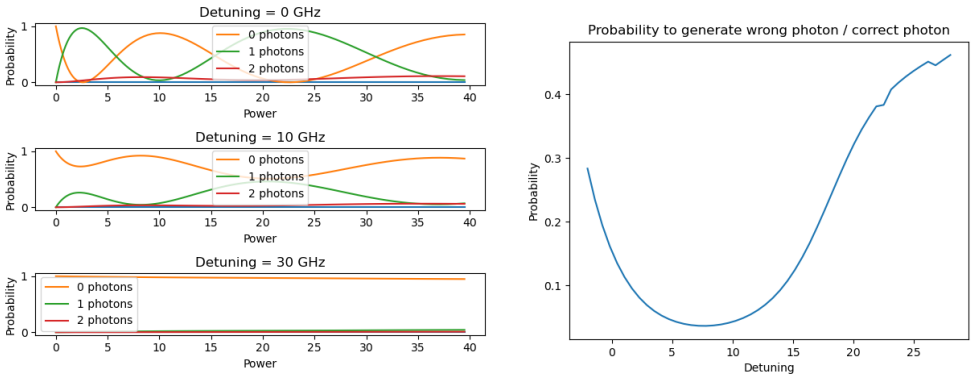

Figure 5: left) *Simulation of an excitation pulse with a Gaussian envelope with FWHM of* 30*ps. The first case is when the excitation laser frequency is on resonance in which case the one photon component should ideally reach 1. The other cases are with detuned excitation laser frequencies where ideally the 0 photon component remains at 1.* ***right)*** *The probability to generate a photon in the (10 + x) GHz detuned case divided by the x GHz case as a function of x. The power of the pulses are set to the pi-power for the 0 GHz detuning case. The lowest point is at* $7.5GHz$ *which is half of the bandwidth of the laser pulse.*

a double excitation is already 0.05. However, for 30 GHz the probability to produce a wrong photon is negligible. The best solution for this is to make a new wafer without this error since the pulse could be shortened in this case yielding a low multi-photon component and low probability of exciting a wrong spin state. In principle this effect can also be lowered by red detuning the excitation laser and post selecting on results where a photon was detected. This will have a different effect on the wrong photon generation than on the correct generation and thus a sweet spot can be found which minimizes the effective error probability (probability of generating wrong photon divided by the probability to generate a correct photon). This sweet spot turns out to be at 7.5 GHz with an effective error probability of 0.036, however this comes at the cost of lowering the rate of state generation by more than half per photon in the state. This reasoning also seems to be wrong since when the simulation is run both lowering the excitation power to drive less than a pi-pulse and detuning by 7.5 GHz seems to lower the state fidelity. Thus there is either a problem with this simulation, the monte carlo state simulation or the reasoning.

4 Experimental setup

In this section the setup to generate and measure the photon states is described. The setup consists of three parts, the wafer, the lasers and the interferometer.

4.1 Wafer

The layout of the wafer itself is described in figure 4 and the wafer is located in a cryostat which is kept at a temperature of 4K to minimize noise from phonons. As mentioned in section 3.7 the current wafer is actually manufactured wrong. The waveguide was build perpendicular to the correct orientation which caused the indirect transition to be Purcell enhanced instead of the direct transition. In turn, this results in the indirect transition being the cycling transition. This is not a problem in itself since the physics are the same for the two transitions. However, the detuning between the two indirect transitions are ≈ 10 GHz while for the direct transitions it is ≈ 30 GHz. Since the only mechanism really affected by this detuning is the photon generation protocol which uses the cycling transition, this affects the fidelity of the generated state.

A voltage source applies a voltage across the device of approximately 1.31 V however this voltage is changed regularly to tune the QD into resonance with the pulsed laser frequency since the laser frequency is much harder to tune. On top of the cryostat is a breadboard with four different laser paths. The position and orientation of each path can be adjusted with mirrors and the polarization of each path is controlled by a PBS/linear polarizer followed by a HWP and a QWP. The power of each path is monitored with a power meter after the PBS/polarizers. The power meters are connected to PIDs to stabilize the power. The PIDs control the laser powers using the AOM setups described in the laser section. All paths are combined into a single beam using beam splitters which goes through a lens on the top part of the cryostat to access the wafer. The output light from the grating coupler of the wafer is spatially separated from the laser paths using a right angle mirror and polarized with opposite polarization from the excitation laser to make separation, of scattered excitation light and signal, easier. The signal is collected into a fiber on the breadboard using a set of mirrors and a linear polarizer to filter out scattered excitation laser light. The collected light is sent to the interferometer to be able to interfere the early and late pulses.

4.2 Lasers

There are four lasers, one for each path. Path 1 is used for excitation of the QD. For this path a Mira 900 laser from Coherent (MIRA) is used to generate ultra short pulses with FWHM of approximately 4 ps resonant to the cycling transition of 316.2725 THz. These pulses are generated at a repetition rate of 72.5978 MHz. Since the MIRA laser has a very large bandwidth of around 78 GHz it is reflected off a volume Bragg grating resulting in a bandwidth of around 15 GHz. Since the pulses are close to Fourier limited this has the downside of broadening the pulse width to 30 ps, but this is a trade off which must be done. This laser is then sent through a fast AOM setup to be able to pick which pulses are used and to control the power of them. Finally this laser is sent to the interferometer to split it into an early and a late pulse.

Path 2 is used to rotate the spin state. This is a CTL laser from TOPTICA photonics which is red detuned from the excitation transition by 650 GHz. This laser is sent through an AOM setup to control the power and then an EOM which is modulated by a RF signal which modulates the intensity of the laser harmonically at a frequency of 10 GHz corresponding to half the spin state energy splitting. The phase of this RF signal can be controlled to determine the axis of rotation as described in section 3.4.

Path 3 and 4 are used for initialization and readout of the spin state. They are both DLPro lasers from TOPTICA photonics. The initialization laser is resonant to the non-cycling transition of 316.2825 THz while the readout laser is resonant to the cycling transition of 316.2725 THz. Both lasers are sent through their own AOM setups to control their powers independently.

4.3 Interferometer

The last part of the setup is the interferometer which is described in figure 6. The MIRA laser pulses are sent into the interferometer to split them into early and late photons with predictable relative phases. The photons generated on the wafer by the QD are sent through the same interferometer allowing for self stabilization of the path lengths. Background photons are filtered out using 3 GHz bandwidth etalons and using the EOM the path of each individual photon can be chosen. However, this was not working yet so the polarization of the collected photons was set to give each of them a 50% chance to go though each arm. This essentially means that the measurement basis was chosen at random between the z-basis and a single direction in the xy-plane. Each of the outputs of the interferometer are sent to individual superconduction nanowire single photon detectors (SNSPD) which sends a voltage pulse to a time tagger from Swabian Instruments saving all of thetime stamps of the photon clicks. This design does make it impossible to measure different photonic qubits in the same state along different axes in the xy-plane.

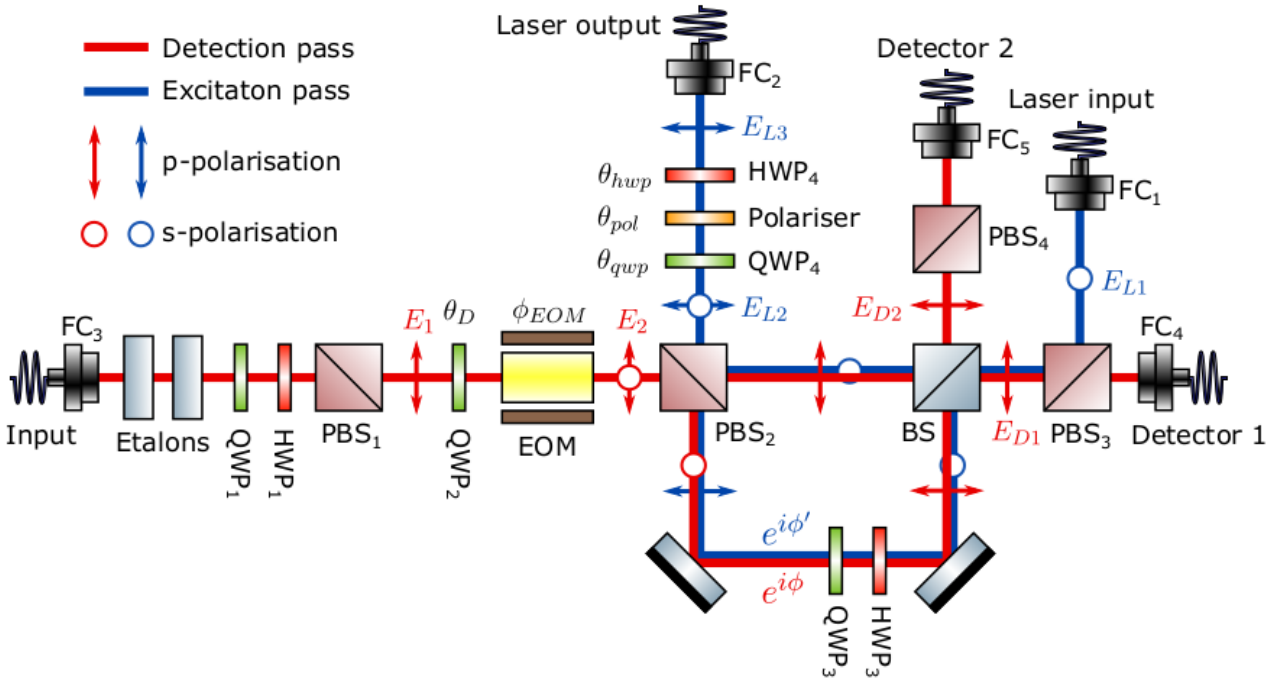

Figure 6: *The interferometric setup. The MIRA laser is sent in through the laser input at vertical polarization and split into two pulses at the BS. One pulse (early) goes through the short arm of the interferometer while the other (late) goes through the long arm and is rotated to a horizontal polarization. The two pulses are both combined into a single path on PBS2 and both are rotated to circlular polarizations and by use of a polarizer the pulses are collected at the laser output with the same polarization. The direction of the polarizer can be changed to set the relative phase between the pulses. The collected photons are sent in though the input and unwanted photons are filtered away in the two etalons. The polarization is then controlled using QWP1, HWP1 and PBS1, the resulting polarization is in the vertical direction. This is sent through QWP2 and the EOM the allow each photon to have a deterministic polarization. The early/late pulses can either be sent through the short/long arms to measure which pulse the photon arrives in or through the long/short arm to interfere on the BS and measure the phase between them. The two outputs of the BS are collected into individual fibers. The figure is taken from Martin Hayhurst Appel's PhD thesis [1]*

5 PID optimization

In the lab PIDs are used for a variety of different tasks. In this work PIDs are used to to lock the laser powers and to lock the temperature of various parts of the setup. This includes the cryo breadboard, the TBI EOM and the etalon filters. While the temperature locking of the etalon filters works well due to the good insulation of them, the locking of the EOM and the breadboard are very tricky. This is because they are not very well insulated and thus they are very sensitive to changes the the environmental temperature. On top of this these systems have a large delay between changing the heating output and detecting the resulting temperature change in the input. This may cause large oscillations in the temperature if the PID values are not set correctly and thus a precise fine tuning of the parameters is essential. The other issue is the time is takes to stabilize, since heat transfers slowly this may take 10-30 minutes which means each set of parameters needs at least half an hour to test. Since an optimization requires testing a lot of parameters, this would take a really long time. In the following the breadboard PID will be used as an example since this is easier to stabilize. The EOM PID could also be optimized this way but it has a lot of issues. First it cools the EOM down instead of heating it up, doing this heats up the environment which makes it even harder and more unstable to cool down. The second issue is its close proximity to some of the AOM setups. These produce a lot of heat and can change the temperature of the environment a lot depending on how hard they work. This change can be enough to go beyond the cooling capacity of the EOM making it impossible to stabilize without regularly changing the setpoint.

A solution to the issue of slow optimization is to simulate the problem instead. As a model for the system it is assumed that the the volume the PID must stabilize has a uniform temperature of $T(t) \equiv T_0 + \delta T(t)$ where T_0 is the setpoint. The outside temperature is $T_a(t) \equiv T_0 + \Delta T_a(t) + \delta T_a(t)$ where the average of δT_a over short times is 0 and ΔT_a changes slowly. The coefficient of heat transfer is k. Thus the heat exchange per unit time between the stabilized volume and the reservoir is

$$H_a(t) \equiv \dot{T}(t) = -k(\delta T(t) - \Delta T_a(t) - \delta T_a(t)). \tag{77}$$

For simplicity it is assume that on average $|\delta T_a| >> |\delta T|$ yielding $H_a(t) \approx k(\Delta T_a + \delta T_a)$. The PID will take in the setpoint and current temperature and produce an output $V(t)$ which is capped to be within the region $V_{min} \leq V \leq V_{max}$. This output results in the heating of the stabilized volume of $H_V(t) = SV(t)$. Finally the time delay between applying a change of temperature until the PID can detect it is R yielding

$$\begin{aligned} V(t) &= -P\delta T(t-R) - I\int_{-\infty}^{t} dt\delta T(t-R) - D\frac{\partial \delta T(t-R)}{\partial t} \\ \dot{\delta T}(t) &= H_a(t) + H_V(t), \end{aligned} \tag{78}$$

where P, I and D are the constants that must be determined for the optimal stabilization. To figure out what PID values should be the system is simulated with a lot of different values. For each simulation the loss function is given by the log of the root mean square of the temperature fluctuation $L(P,I,D) = \log\sqrt{\int_{-\infty}^{\infty} dt(\delta T(t))^2}$.

The only non-trivial part of the simulation is the ambient temperature. δT_a is simulated by doing a Gaussian random walk and $\Delta T_a(t) = a + A\cos(\omega(t - t_0))$.

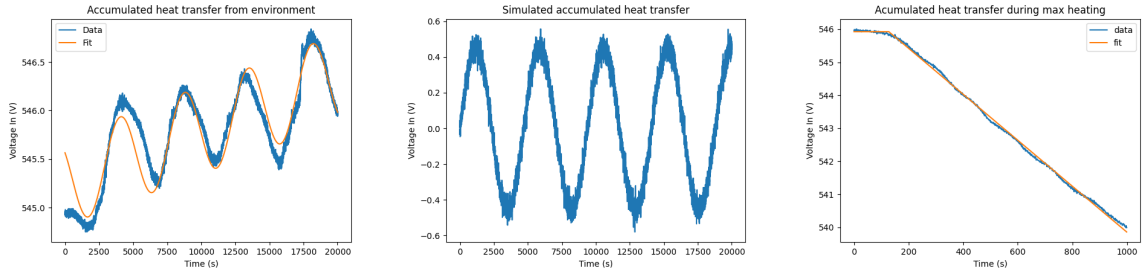

Figure 7: Left) *A 20 hour recording of the ambient temperature fitted with the function* $a + bt + A\sin(\omega(t - t_0))$. ***Middle)*** *A simulation of the ambient temperature, the long time scale is a harmonic oscillation, the linear part has been removed, and the short time oscillations are given by a Gaussian random walk. There are differences between the simulated temperature and the real one but they are not significant.* ***Right)*** *The temperature during max heating. It starts heating at* $t = 0$ *and the delay until the slope begins is* R.

To determine the parameters for the simulation (R, S and $T_a(t)$) some preliminary measurements of the physical system is done. First the PID is allowed to stabilize such that the average output to keep the temperature stable is found. Then the PID is set to this constant V_{mean} for a long time. During this period the internal temperature is recorded as $T_r(t)$. In post processing the heat curve is found from $H_a(t) = \dot{T}_r(t)$. The low frequency variations of T_a is then found with a fit of the function $a + bt + A\cos(\omega(t - t_0))$ to the data. After this the step size of the random walk is set such that the mean variance is equal to the mean variance of $T_r - T_a$. During the next measurement the PID will heat at max output. The recorded temperature $T_h(t)$ is fitted with a constant for $t < R$ and then a linear equation for $t > R$ with a slope of s. Doing this yields R and $S = \frac{s}{V_{max} - V_{mean}}$. These measurements are shown in figure 7.

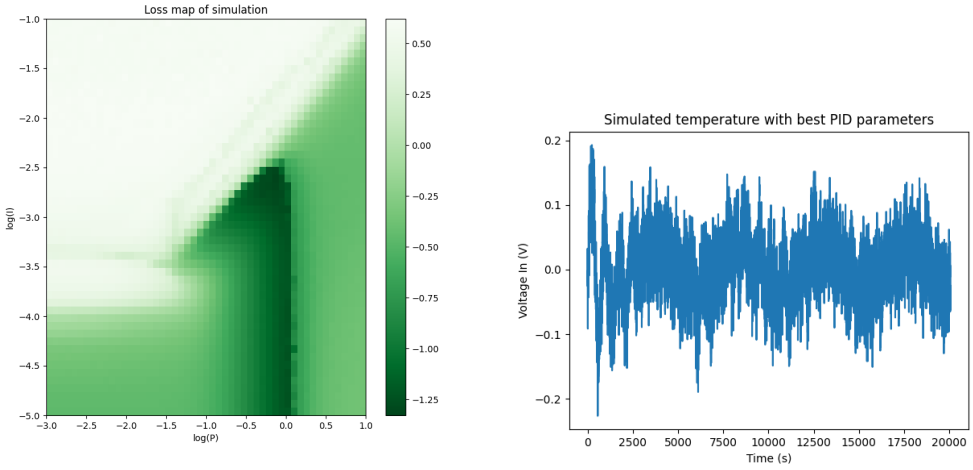

Figure 8: left) *The loss map of the PID scan, D is set to 0 since it is not useful with such a large delay, the loss function is log RMS. The top-left region is an unstable part of parameter space where the PID will overcompensate and start oscillating out of control.* ***right)*** *A sample curve for the stabilized temperature using the best PID values of* $P = 0.76$*,* $I = 0.0025$ *and* $D = 0$*.*

Doing the analysis and the simulation yields the results of figure 8 which shows that if I is too large or P is too small then the PID will overcompensate resulting in diverging behavior. But it also shows that there is a stable part of parameter space and at the best spot the simulated temperature looks very similar to what is seen in the lab. The best PID values was found to be $P = 0.76$, $I = 0.0025$ and $D = 0$ which is very close to the $P = 0.7$, $I = 0.0015$ and $D = 0$ that was found in the lab. This shows that the simulation seems to work well but unfortunately it seems that the PID cannot be optimized any further. There are two main problems. The first is the large long time scale oscillations, these can only be compensated for to a certain degree since higher I-value would lead to divergent oscillations. To solve this the outside temperature must be kept more constant, the system must be better insulated or some automatic oscillatory response must be applied on top of the PID. The other main problem is the large delay of $R = 128s$, since the PID cannot detect any change until two minutes after they occured this limits the responsiveness a lot. It also causes a lot of oscillatory behaviors since it will keep responding for two minutes after the response should have stopped. To solve this a different type of stabilization algorithm should be used, one which takes the delay into account. One such method was simulated and showed promising results for model data, however, on the real data it was not able to improve the locking. More work is needed to improve this.

6 Measurement based quantum computing and Deutsch's algorithm

6.1 States

Before discussing the operators that are needed for the further discussion the basis states are first introduced. Any single qubit system can be described by a basis of 2 states, and any multi-qubit system can be described by combining single qubit bases. The most simple basis from which everything else can be described is the z-basis ($|0\rangle$, $|1\rangle$).

Another important basis is the χ-basis. This is the basis in the xy-plane at an angle χ relative to the x-axis.

$$|\chi_{\pm}\rangle = \frac{1}{\sqrt{2}}\Big(\exp\left(-i\frac{\chi}{2}\right)|0\rangle \pm \exp\left(i\frac{\chi}{2}\right)|1\rangle\Big), \tag{79}$$

with the property

$$|\chi_{-}\rangle = i\left|(\chi+\pi)_{+}\right\rangle. \tag{80}$$

A special case of this is the x-basis which is described as

$$|\pm\rangle = \frac{1}{\sqrt{2}}(|0\rangle \pm |1\rangle). \tag{81}$$

6.2 Operators

Next the important operators are introduced. First all the single qubit operators will be introduced and later the 2-qubit operators. Some important properties of theses operators are also discussed.

6.2.1 Single qubit operators

The single qubit operators are operators that only acts on a single qubit, these can always be decomposed into a series of rotation operators which are generated by the Pauli operators.

Just for completeness the identity operator is defined as

$$\hat{I} \equiv |0\rangle\langle 0| + |1\rangle\langle 1| = |\chi_{+}\rangle\langle\chi_{+}| + |\chi_{-}\rangle\langle\chi_{-}|. \tag{82}$$

The Pauli operators are the generators for the rotation operators and perform simple π rotations themselves. They are defined as

$$\begin{aligned}
\hat{\sigma}^x &\equiv |1\rangle\langle 0| + |0\rangle\langle 1| = |+\rangle\langle +| - |-\rangle\langle -| \\
\hat{\sigma}^y &\equiv i(|1\rangle\langle 0| - |0\rangle\langle 1|) = i(|+\rangle\langle -| - |-\rangle\langle +|) \\
\hat{\sigma}^z &\equiv |0\rangle\langle 0| - |1\rangle\langle 1| = |+\rangle\langle -| + |-\rangle\langle +| \\
\hat{\vec{\boldsymbol{\sigma}}} &= \hat{\sigma}^x\hat{\boldsymbol{x}} + \hat{\sigma}^y\hat{\boldsymbol{y}} + \hat{\sigma}^z\hat{\boldsymbol{z}}.
\end{aligned} \tag{83}$$

Some important properties include

$$\begin{aligned}\left(\hat{\sigma}^i\right)^2 &= \hat{I} \\ \hat{\sigma}^i\hat{\sigma}^j &= i\varepsilon^{ijk}\hat{\sigma}^k,\end{aligned} \tag{84}$$

where ε^{ijk} is the Levi-Civita symbol. Using 84 it is also possible to derive

$$\begin{aligned}&(a\hat{\sigma}^x + b\hat{\sigma}^y + c\hat{\sigma}^z)^2 = a^2(\hat{\sigma}^x)^2 + b^2(\hat{\sigma}^y)^2 + c^2(\hat{\sigma}^z)^2 \\ &+ ab(\hat{\sigma}^x\hat{\sigma}^y + \hat{\sigma}^y\hat{\sigma}^x) + ac(\hat{\sigma}^x\hat{\sigma}^z + \hat{\sigma}^z\hat{\sigma}^x) + bc(\hat{\sigma}^y\hat{\sigma}^z + \hat{\sigma}^z\hat{\sigma}^y) = \left(a^2 + b^2 + c^2\right)\hat{I}.\end{aligned} \tag{85}$$

The rotation operators rotate a qubit around some axis of rotation. The operators are generated by the Pauli operators as

$$\hat{R}(\hat{\boldsymbol{r}}, \theta) = \exp\left(-i\hat{\boldsymbol{r}}\cdot\hat{\vec{\boldsymbol{\sigma}}}\frac{\theta}{2}\right), \tag{86}$$

where $\hat{\boldsymbol{r}}$ is the rotation axis and θ is the rotation angle. Given this generator two special cases can be derived. The first is a rotation around the z-axis

$$\hat{R}^z(\theta) \equiv \hat{R}(\hat{\boldsymbol{z}}, \theta) = \exp\left(-i\hat{\sigma}^z\frac{\theta}{2}\right) = \exp\left(-i\frac{\theta}{2}\right)|0\rangle\langle 0| + \exp\left(i\frac{\theta}{2}\right)|1\rangle\langle 1|. \tag{87}$$

The second is a rotation in the xy-plane with a rotation axis at an angle χ relative to the x-axis

$$\begin{aligned}&\hat{R}^\chi(\theta) \equiv \hat{R}(\cos(\chi)\hat{\boldsymbol{x}} + \sin(\chi)\hat{\boldsymbol{y}}, \theta) = \exp\left(-i(\cos(\chi)\hat{\sigma}^x + \sin(\chi)\hat{\sigma}^y)\frac{\theta}{2}\right) \\ &= \sum_{n=0}^{\infty}\frac{1}{(2n)!}\left(-i(\cos(\chi)\hat{\sigma}^x + \sin(\chi)\hat{\sigma}^y)\frac{\theta}{2}\right)^{2n} + \sum_{n=0}^{\infty}\frac{1}{(2n+1)!}\left(-i(\cos(\chi)\hat{\sigma}^x + \sin(\chi)\hat{\sigma}^y)\frac{\theta}{2}\right)^{2n+1} \\ &- i(\cos(\chi)\hat{\sigma}^x + \sin(\chi)\hat{\sigma}^y)\sum_{n=0}^{\infty}(-1)^n\frac{\left(\frac{\theta}{2}\right)^{2n+1}}{(2n+1)!}\left((\cos(\chi)\hat{\sigma}^x + \sin(\chi)\hat{\sigma}^y)^2\right)^n \\ &= \sum_{n=0}^{\infty}(-1)^n\frac{\left(\frac{\theta}{2}\right)^{2n}}{(2n)!} - i(\cos(\chi)\hat{\sigma}^x + \sin(\chi)\hat{\sigma}^y)\sum_{n=0}^{\infty}(-1)^n\frac{\left(\frac{\theta}{2}\right)^{2n+1}}{(2n+1)!} \\ &= \cos\left(\frac{\theta}{2}\right)(|0\rangle\langle 0| + |1\rangle\langle 1|) - i\sin\left(\frac{\theta}{2}\right)(\exp(-i\chi)|0\rangle\langle 1| + \exp(i\chi)|1\rangle\langle 0|).\end{aligned} \tag{88}$$

It is clear that the z-basis are eigenstates to the z-rotation with eigenvalues $(\exp\left(-i\frac{\theta}{2}\right), \exp\left(i\frac{\theta}{2}\right))$ for $(|0\rangle, |1\rangle)$. It can also easily be verified that $(|\chi_+\rangle, |\chi_-\rangle)$ are eigenstates to $\hat{R}^\chi$ with eigenvalues $(\exp\left(-i\frac{\theta}{2}\right), \exp\left(i\frac{\theta}{2}\right))$. It is also easy to verify that $\hat{R}^z(\theta)|\chi_\pm\rangle = \left|(\chi+\theta)_\pm\right\rangle$ as is expected from a z-rotation. Two special cases of the χ-rotation are

$$\begin{aligned}\hat{R}^x(\theta) \equiv \hat{R}^0(\theta) &= \cos\left(\frac{\theta}{2}\right)(|0\rangle\langle 0| + |1\rangle\langle 1|) - i\sin\left(\frac{\theta}{2}\right)(|0\rangle\langle 1| + |1\rangle\langle 0|) \\ \hat{R}^y(\theta) \equiv \hat{R}^{\frac{\pi}{2}}(\theta) &= \cos\left(\frac{\theta}{2}\right)(|0\rangle\langle 0| + |1\rangle\langle 1|) - \sin\left(\frac{\theta}{2}\right)(|0\rangle\langle 1| - |1\rangle\langle 0|).\end{aligned} \tag{89}$$

The last special case is the Hardamard operator. This operator is defined as

$$\begin{aligned}\hat{H} &\equiv |0\rangle\langle 0| + |0\rangle\langle 1| + |1\rangle\langle 0| - |1\rangle\langle 1| = |+\rangle\langle 0| + |-\rangle\langle 1| \\ &= |0\rangle\langle +| + |1\rangle\langle -| = |+\rangle\langle +| + |-\rangle\langle +| + |+\rangle\langle -| - |-\rangle\langle -|\,.\end{aligned} \tag{90}$$

This operator just switches the z-basis to the x-basis. It can be decomposed into rotation operators as

$$\hat{H} = i\hat{R}^y\Big(\frac{\pi}{2}\Big)\hat{R}^z(\pi). \tag{91}$$

Some important properties are

$$\begin{aligned}\hat{H}^2 &= \hat{I} \\ \hat{H}\hat{\sigma}^z\hat{H} &= \hat{\sigma}^x \\ \hat{H}\hat{\sigma}^x\hat{H} &= \hat{\sigma}^z.\end{aligned} \tag{92}$$

6.2.2 2-qubit operators

Two important 2-qubit operators will be defined. 2-qubit operators are important since with a single 2-qubit operator and all rotation operators one has an universal gate set. These following two operators are the ones that will be used in the following section. The first operator is the control phase operator since this is important for theoretical calculations. It is defined as flipping the phase if both qubits are in the $|1\rangle$ state.

$$\hat{U}_{01}^{cz} \equiv |00\rangle\langle 00|_{01} + |01\rangle\langle 01|_{01} + |10\rangle\langle 10|_{01} - |11\rangle\langle 11|_{01} = |0\rangle\langle 0|_0\,\hat{I}_1 + |1\rangle\langle 1|_0\,\hat{\sigma}_1^z = |0\rangle\langle 0|_1\,\hat{I}_0 + |1\rangle\langle 1|_1\,\hat{\sigma}_0^z, \tag{93}$$

where the subscript defines what qubits are being referred to. It is also easily verified that

$$\Big(\hat{U}_{01}^{cz}\Big)^2 = \hat{I}. \tag{94}$$

Next the control not operator is introduced as this is used experimentally to generate the states. The link between these two operators are also discussed. The control not operator flips the second (target) qubit if the first (input) qubit is $|1\rangle$

$$\hat{U}_{01}^{cnot} \equiv |00\rangle\langle 00|_{01} + |01\rangle\langle 01|_{01} + |10\rangle\langle 11|_{01} + |11\rangle\langle 10|_{01} = |0\rangle\langle 0|_0\,\hat{I}_1 + |1\rangle\langle 1|_0\,\hat{\sigma}_1^x. \tag{95}$$

From the last form it is clear that

$$\begin{aligned}\Big(\hat{U}_{01}^{cnot}\Big)^2 &= \hat{I} \\ \hat{U}_{01}^{cnot} &= \hat{H}_1\hat{U}_{01}^{cz}\hat{H}_1.\end{aligned} \tag{96}$$

So using Hardamard it is possible to transform between control phase and control not.

6.3 Graph state

A graph state is a multi qubit state. The N qubit graph state is defined from a set of pairs of qubits which is called S. The qubits are labelled as 0, 1, ..., $N-1$. Any pairs of qubits are said to be neighbours. Then the graph state is defined as

$$|\psi\rangle = \prod_{\{nm\}\in S} \hat{U}^{cz}_{nm} |+\rangle^{\otimes N} . \tag{97}$$

6.3.1 Identities

There are a few important identities for graph states which can be used to rewrite expressions. Each of them can easily be shown with straight forward calculations.

$$\begin{aligned}
&\hat{\sigma}^z_0 \hat{\sigma}^x_1 \hat{U}^{cz}_{01} |++\rangle_{01} = \hat{U}^{cz}_{01} |++\rangle_{01} \\
&\hat{\sigma}^z_0 \hat{\sigma}^z_1 \hat{U}^{cz}_{01} |++\rangle_{01} = -\hat{\sigma}^x_0 \hat{\sigma}^x_1 \hat{U}^{cz}_{01} |++\rangle_{01} \\
&\hat{H}_0 \hat{H}_1 \hat{U}^{cz}_{01} |++\rangle_{01} = \hat{U}^{cz}_{01} |++\rangle_{01} \\
&\hat{H}_0 \hat{H}_2 \hat{U}^{cz}_{01} \hat{U}^{cz}_{02} |+++\rangle_{012} = \hat{U}^{cz}_{20} \hat{U}^{cz}_{21} |+++\rangle_{012} .
\end{aligned} \tag{98}$$

6.3.2 Linear cluster state

A special case of a graph state is the linear cluster state where N qubits are placed on a line and each qubit is connected with its neighbour(s) on the line.

$$\begin{aligned}
S &= \{(i, i+1) \mid i \in \mathbb{N} \wedge i < N-1\} \\
|\psi\rangle &= \prod_{n=0}^{N-2} \hat{U}^{cz}_{nn+1} |+\rangle^{\otimes N} .
\end{aligned} \tag{99}$$

6.4 Measurement based quantum computing

The final goal for creating the graph states is to be able to perform quantum computations with them. This will be done by performing measurements on the state. By performing measurements on qubits in the graph state it effectively propagates single qubit rotations to the neighbours of the measured qubits. This combined with the existing control phase operators from initialization means that any quantum algorithms can be implemented if the initial state is large enough and there are enough connections between qubits. This work will focus on the linear cluster state which is not a universal quantum computing resource but is much simpler to create in the lab.

When performing measurement based quantum computing the only possible operations that can be done on the state after initialization is measurements. The implementation of the algorithm comes down to the choice of measurement bases. Due to the probabilistic nature of measurements the result will be random. This is fixed by feed forward operations where the next measurement basis may depend on the result of the previous measurement and with post corrections to the result depending on the measurement results. The bases which can be chosen in this work are the z-basis and any χ-basis. With these it is possible to implement any algorithm.

6.4.1 z measurements

First the effects of z-measurements are shown. The possible measurement results are ($|0\rangle$ and $|1\rangle$) and the initial state is assumed to be

$$|\psi\rangle = \prod_{\{0n\}\in S} \hat{U}^{cz}_{0n} \hat{R}_n \hat{R}_0 \, |+\rangle^{\otimes N} \,, \tag{100}$$

where $\hat{R}_n$ is some arbitrary single qubit rotation on the n'th qubit and the measurement is performed on qubit 0. The unormalized states after the measurement is

$$\begin{aligned} |\psi_0\rangle \equiv \langle 0|_0 \, |\psi\rangle &= \prod_{\{0n\}\in S} \hat{R}_n \, |+\rangle^{\otimes (N-1)} \, \langle 0| \, \hat{R}_0 \, |+\rangle_0 \\ |\psi_1\rangle \equiv \langle 1|_0 \, |\psi\rangle &= \prod_{\{0n\}\in S} \sigma^z_n \hat{R}_n \, |+\rangle^{\otimes (N-1)} \, \langle 1| \, \hat{R}_0 \, |+\rangle_0 \,, \end{aligned} \tag{101}$$

for the two different measurement results. Thus if the set of all pairs including qubit 0 is defined as S_0, the set of all the other pairs is defined as S_{new}, and the result of the measurement is α then measuring the state

$$|\psi\rangle = \prod_{\{nm\}\in S} \hat{U}^{cz}_{nm} \prod_{n=0}^{N-1} \hat{R}_n \, |+\rangle^{\otimes N} \,, \tag{102}$$

results in the new state

$$|\psi_\alpha\rangle = \prod_{\{nm\}\in S_0} (\hat{\sigma}^z_n)^\alpha \prod_{\{nm\}\in S_{new}} \hat{U}^{cz}_{nm} \prod_{n=1}^{N-1} \hat{R}_n \, |+\rangle^{\otimes (N-1)} \,. \tag{103}$$

The result is that doing a z-measurement removes the measured qubit and any control phase operation on this qubit. It also possibly does a $\hat{\sigma}^z$ rotation on all the neighbours of the measured qubit. As a special case consider the state

$$|\psi\rangle = \hat{U}^{cz}_{01} \hat{U}^{cz}_{12} \hat{U}^{cz}_{23} \, |+\rangle^{\otimes 4} \,, \tag{104}$$

and measure qubit 1 and 2 in the z basis. The resulting state is

$$|\psi_{\alpha_1\alpha_2}\rangle = (\hat{\sigma}^z_0)^{\alpha_1} (\hat{\sigma}^z_3)^{\alpha_2} \, |+\rangle^{\otimes 2} \,, \tag{105}$$

where α_1 and α_2 are the measurement results.

6.4.2 χ measurements

Now the effects of a χ measurement is shown. This can yield the states ($|\chi_+\rangle$ or $|\chi_-\rangle$) which is a bit more complicated. It is assumed that the initial state is

$$|\psi\rangle = \prod_{n=1}^{N} \hat{U}_{0n}^{cz} \hat{R}_0 \, |+\rangle^{\otimes(N+1)} \tag{106}$$

with the arbitrary rotation

$$\begin{aligned} \hat{R}_n &= a \, |0\rangle\langle 0|_n + b \, |1\rangle\langle 0|_n - b^* \, |0\rangle\langle 1|_n + a^* \, |1\rangle\langle 1|_n \\ |a|^2 &+ |b|^2 = 1 \end{aligned} \tag{107}$$

The resulting state after a measurement of qubit 0 is

$$\begin{aligned} |\psi_\pm\rangle &= \frac{1}{\sqrt{2}} \Big(\exp\left(i\frac{\chi}{2}\right) \langle 0|_0 \pm \exp\left(-i\frac{\chi}{2}\right) \langle 1|_0 \Big) \prod_{n=1}^{N} \Big(|0\rangle\langle 0|_0 \, \hat{I}_n + |1\rangle\langle 1|_0 \, \hat{\sigma}_n^z \Big) R_0 \, |+\rangle_0 \, |+\rangle^{\otimes N} \\ &= \frac{1}{2} \Big((a - b^*) \exp\left(i\frac{\chi}{2}\right) |+\rangle^{\otimes N} \pm (b + a^*) \exp\left(-i\frac{\chi}{2}\right) |-\rangle^{\otimes N} \Big) \\ &= \frac{1}{2} (\hat{\sigma}_1^x)^{\alpha_\pm} \hat{H}_1 \hat{R}_1^z(-\chi) \Big((a - b^*) \, |0\rangle_1 \, |+\rangle^{\otimes(N-1)} + (b + a^*) \, |1\rangle_1 \, |-\rangle^{\otimes(N-1)} \Big) \\ &= \frac{1}{2} (\hat{\sigma}_1^x)^{\alpha_\pm} \hat{H}_1 \hat{R}_1^z(-\chi) \prod_{n=2}^{N} \hat{U}_{1n}^{cz} \big((a - b^*) \, |0\rangle_1 + (b + a^*) \, |1\rangle_1 \big) \, |+\rangle^{\otimes(N-1)} \\ &= \frac{1}{\sqrt{2}} (\hat{\sigma}_1^x)^{\alpha_\pm} \hat{H}_1 \hat{R}_1^z(-\chi) \prod_{n=2}^{N} \hat{U}_{1n}^{cz} \hat{R}_1 \, |+\rangle^{\otimes N} , \end{aligned} \tag{108}$$

where $\alpha_+ = 0$ and $\alpha_- = 1$ is the measurement result. The factor $\frac{1}{\sqrt{2}}$ can be removed by normalization and just means that both $|\chi_\pm\rangle$ are equally likely to be measured. There was also nothing special about qubit 1, this could be any of the qubits.

$$|\psi_\pm\rangle = (\hat{\sigma}_1^x)^{\alpha_\pm} \hat{H}_1 \hat{R}_1^z(-\chi) \prod_{n=2}^{N} \hat{U}_{1n}^{cz} \hat{R}_1 \, |+\rangle^{\otimes N} . \tag{109}$$

This means that doing this measurement will transfer the rotation and all of the control phase operators from qubit 0 onto one of its neighbours. After that it will apply a rotation around the z-axis followed by a Hardamard and possibly a Pauli-x operator depending on the measurement result. There are two important special cases of this. The first case is

$$\begin{aligned} |\psi\rangle &= \hat{U}_{01}^{cz} \hat{R}_0 \, |++\rangle_{01} \\ |\psi_\pm\rangle &= (\hat{\sigma}_1^x)^{\alpha_\pm} \hat{H}_1 \hat{R}_1^z(-\chi) \hat{R}_1 \, |+\rangle_1 , \end{aligned} \tag{110}$$

which is how a single qubit rotation can be performed. The next case is

$$\begin{aligned} |\psi\rangle &= \hat{U}_{01}^{cz} \hat{U}_{02}^{cz} \hat{R}_0 \, |+++\rangle_{012} \\ |\psi_\pm\rangle &= (\hat{\sigma}_2^x)^{\alpha_\pm} \hat{H}_2 \hat{R}_2^z(-\chi) \hat{U}_{12}^{cz} \, |++\rangle_{12} , \end{aligned} \tag{111}$$

where a qubit is removed while keeping the entanglement intact. From this another useful example can be derived starting with the state

$$|\psi\rangle = \hat{U}_{01}^{cz}\hat{U}_{12}^{cz}\hat{U}_{23}^{cz}\,|+\rangle^{\otimes 4}, \tag{112}$$

and measure both qubit 1 and 2 in the x-basis.

$$\begin{aligned} |\psi_{\alpha_1\alpha_2}\rangle &= (\hat{\sigma}_0^x)^{\alpha_1}\hat{H}_0(\hat{\sigma}_0^x)^{\alpha_2}\hat{H}_0\hat{U}_{02}^{cz}\,|+\rangle^{\otimes 2} \\ &= (\hat{\sigma}_0^x)^{\alpha_1}(\hat{\sigma}_3^x)^{\alpha_2}\hat{U}_{03}^{cz}\,|+\rangle^{\otimes 2} = (\hat{\sigma}_0^z)^{\alpha_2}(\hat{\sigma}_3^z)^{\alpha_1}\hat{U}_{03}^{cz}\,|+\rangle^{\otimes 2}, \end{aligned} \tag{113}$$

up to a global phase. Thus measuring qubit 1 and 2 in the x basis just propagates a control phase between qubit 0 and 3.

6.5 Deutsch's algorithm

Next the theoretical background for Deutsch's algorithm is discussed. It is a very simple quantum algorithm which revolves around the function

$$f : \{0,1\} \to \{0,1\}. \tag{114}$$

Which just takes in one bit of information and outputs another bit. The problem is then to find out whether the function is constant ($f(0) = f(1)$) or if it is balanced ($f(0) \neq f(1)$). Classically this would take 2 function calls as one would need to evaluate $f(0)$ and $f(1)$. But a quantum algorithm can exploit the fact that only one bit of information is needed which means that 1 function call is enough. Usually Deutsch's algorithm is implemented using an oracle operator which takes in a query and an ancilla qubit. If the state of the query and ancilla qubits are $|q\rangle$ and $|a\rangle$ then the oracle changes the ancilla qubit to be $|a \oplus f(q)\rangle$. In other words, if $f(q) = 1$ then it flips the ancilla qubit. This can be written as operators as

$$\hat{U}^f = (\hat{\sigma}_a^x)^{f(0)}\left(\hat{U}_{qa}^{cnot}\right)^{\beta}, \tag{115}$$

where $\beta = 0$ if the function is constant and $\beta = 1$ if the function is balanced. In this case a slightly different approach is used. Instead of flipping the ancilla qubit the phase is flipped if both the query and ancilla qubit are $|1\rangle$. Then the operator becomes

$$\hat{U}^f = (\hat{\sigma}_a^z)^{f(0)}\left(\hat{U}_{qa}^{cz}\right)^{\beta}. \tag{116}$$

The advantage here is the control phase operator instead of a control not operator, this is useful since the graph states are made up of control phase operators. Now the query qubit is initialized in the $|+\rangle$ state and the ancilla qubit in the $|1\rangle$ state. Then the result of the oracle operator is

$$\hat{U}^f\,|+1\rangle_{qa} = (\hat{\sigma}_a^z)^{f(0)}\left(\hat{U}_{qa}^{cz}\right)^{\beta}|+1\rangle_{qa} = (-1)^{f(0)}\left(|0\rangle_q + (-1)^{\beta}\,|1\rangle_q\right)|1\rangle_a\,. \tag{117}$$

Thus if the function is constant the query qubit stays in the $|+\rangle$ state while if the function is balanced the query qubit is flipped to $|-\rangle$. Therefor to get the result of the algorithm the query qubit is just measured in the x-basis. It is also worth noting that the value of $f(0)$ does not affect the result since it just applies a global phase.

6.5.1 Physical implementation

All algorithms in this chapter has been developed by Love Alexander Mandla Pettersson and Anders Søndberg Sørensen.

The goal is to implement this algorithm in a linear cluster state. In principle a 5 qubit linear cluster state is needed to implement the algorithm. Qubit 0 will be the query qubit, qubit 1 and 2 are the oracle, qubit 3 will be the ancilla qubit and qubit 4 is the ancilla initialization.

The implementation of the constant oracle would be to measure qubit 1 and 2 in the z-basis to sever the entanglement. For the balanced oracle they will both be measured in the x-basis to propagate the entanglement. The initialization qubit will be measured in the negative x-basis to convert the ancilla qubit to the $|1\rangle$ state. Then the query qubit will be measured in the x-basis to measure what configuration the oracle is in.

For the constant case the oracle will perform the operation of equation 105 yielding $|\psi_0\rangle$ apart from the initialization qubit

$$|\psi_0\rangle = (\hat{\sigma}_0^z)^{\alpha_1}(\hat{\sigma}_3^z)^{\alpha_2}|+\rangle^{\otimes 2}, \tag{118}$$

where $\alpha_i = 0$ if qubit i was measured to be $|0\rangle$ ($|+\rangle$) if measured in the z (x) basis and $\alpha_i = 1$ if qubit i was measured to be $|1\rangle$ ($|-\rangle$) if measured in the z (x) basis. For the balanced case equation 113 yields

$$|\psi_1\rangle = (\hat{\sigma}_0^z)^{\alpha_2}(\hat{\sigma}_3^z)^{\alpha_1}\hat{U}_{03}^{cz}|+\rangle^{\otimes 2} \tag{119}$$

The oracle will then return two bits of information to be used to correct the results. The first bit is a, if the function is constant then $a = \alpha_1$ and if the function is balanced then $a = \alpha_2$. Similarly, the second bit of information is b and for a constant function it returns $b = \alpha_2 \oplus f(0)$ and for a balanced function $b = \alpha_1 \oplus f(0)$. The oracle is still a black box since it can potentially give the same outputs for all functions. The initialization is done by measuring qubit 4 in the negative x-basis with $\alpha_4 = 0$ for $|-\rangle$ and $\alpha_4 = 1$ for $|+\rangle$

$$|\psi\rangle = (\hat{\sigma}_0^z)^a(\hat{\sigma}_3^z)^{b\oplus f(0)}\left(\hat{U}_{03}^{cz}\right)^{\beta}(\hat{\sigma}_3^x)^{\alpha_4}|+1\rangle_{03}, \tag{120}$$

where $\beta = 0$ for a constant function and $\beta = 1$ for a balanced function. It is clear that this is Deutsch's algorithm if $a = b = \alpha_4 = 0$. But of course this cannot be guaranteed. To fix this some post processing must be applied. To see this evaluate the state up to a global phase

$$|\psi\rangle = (\hat{\sigma}_0^z)^a (\hat{\sigma}_3^z)^{b\oplus f(0)} \left(\hat{U}_{03}^{cz}\right)^\beta |+, 1\oplus\alpha_4\rangle_{03} = \left|(\pm)^{[\beta(1\oplus\alpha_4)]\oplus a}, 1\oplus\alpha_4\right\rangle_{03}, \tag{121}$$

where the notation $(\pm)^n$ means + if $n = 0$ and - if $n = 1$. Thus measuring qubit 0 in the x-basis will yield the result

$$\alpha_0 = [\beta(1\oplus\alpha_4)]\oplus a. \tag{122}$$

From this it can be seen that if qubit 4 was measured to be $|-\rangle$ then $\beta = a\oplus\alpha_0$. Since a measurement result of $|+\rangle$ on qubit 4 would make it impossible to find β on average the algorithm must be run twice, but this can be circumvented by creating states until it was initialized correctly and then call the oracle. Then the oracle need only be run once. The second option is to modify the oracle such that it also takes in the initialization result as a feed forward parameter. Then if this value is 1 (it measured $|+\rangle$) then it will flip the measured result of qubit 3.

It is also clear from equation 122 that measuring qubit 4 also measures qubit 3 due to the entanglement. Therefor, it is possible to skip qubit 4 and just measure qubit 3 directly in the negative z-basis.

6.5.2 3-qubit Deutsch's algorithm

In the physical system of this work only 3 qubits were able to be generated with decent fidelity and thus Deutsch's algorithm must be shrunk to fit. To do this notice that measuring the ancilla qubit in the $|1\rangle$ state just flips the measurement result for qubit 2 if done in the x-basis, therefore it is possible to remove the ancilla qubit. Then the new algorithm is to measure qubit 1 in the positive z basis (constant) or qubit 2 in the negative x basis (balanced) and the query qubit in the x basis. The other oracle qubits needs not be measured since the result of the measurement does not influence the query qubit. The resulting output of the oracle is $a = \alpha_1$ (constant) and $a = \alpha_2$ (balanced). Then the final result is

$$|\psi\rangle = \left|(\pm)^{\beta\oplus a}\right\rangle_0. \tag{123}$$

From this the type of function can be found from $\beta = a\oplus\alpha_0$ just like for the 4-qubit version.

6.5.3 The problem

However, there are a problem, it is also possible to send in a product state of the type $|+0\rangle_{21}$ to the oracle. Then if the oracle is constant it returns $a = 0$ and if the oracle is balanced it returns $a = 1$ allowing the result to be read directly. This issue cannot be solved with a 3-qubit state but can be solved with the 4-qubit state. To solve it imagine 2 players playing a game. Player one is the oracle and player two has to figure out what function is implemented in the oracle. The rules are that first player two generates a state, then player one tells player two if they need to determine if the function is constant or balanced or if they need to find $f(0)$. After this the state is measured by player two who gives player one instructions on what measurement results to flip and finally

player one does their measurements and return the values a and b. This cannot simply be solved using a product state since such a state can only solve one of the problems in which case player one picks the other ploblem to ask.

To solve it player two prepares the 4-qubit linear cluster state. qubit 1 and 2 are given to player one just like before. If player one asks for constant or balanced then the algorithm is implemented as before. Qubit 3 is measured in the z-basis and if $|0\rangle$ is measured player two tells player one to flip the result of qubit 2. Then qubit 0 is measured in the x-basis and the result is given by $\beta = a \oplus \alpha_0$ where α_0 is 0 for the $|+\rangle$ state. On the other hand, if player one asks for $f(0)$ player two measures qubit 0 in the z-basis and tells player one to flip the result of qubit 1 if they measured $|1\rangle$. Then they measure qubit 3 in the x-basis and the result is given by $f(0) = b \oplus \alpha_3$ where α_3 is 0 if qubit 3 is measured in the $|+\rangle$ state.

6.6 Theoretical state generation

In this section the protocols to generate GHZ and linear cluster states are explored. In these protocols it is assumed that any single qubit operation on qubit 0 can be performed and a control not operator between qubit 0 and any other qubit (U_{0n}^{cnot}) can also be performed. It is also assumed that the initial state is $|0\rangle^{\otimes N}$.

6.6.1 GHZ state

First the GHZ state generation is explored. The GHZ state is a very simple state which can also be generated from a graph state with some Hardamard operations.

$$|GHZ\rangle = |0\rangle^{\otimes N} + |1\rangle^{\otimes N} = \prod_{n=1}^{N-1} \hat{H}_n \prod_{n=1}^{N-1} \hat{U}_{0n}^{cz} |+\rangle^{\otimes N}. \tag{124}$$

The GHZ state can then be generated by first using a hardamard operator on qubit 0 and then control not between qubit 0 and all other qubits

$$\prod_{n=1}^{N-1} \hat{U}_{0n}^{cnot} \hat{H}_0 |0\rangle^{\otimes N} = \prod_{n=1}^{N-1} U_{0n}^{cnot} \hat{H}_n \hat{H}_n \hat{H}_0 |0\rangle^{\otimes N} = \prod_{n=1}^{N-1} \hat{H}_n \prod_{n=1}^{N-1} \hat{U}_{0n}^{cz} |+\rangle^{\otimes N} = |GHZ\rangle. \tag{125}$$

To evaluate if this state is actually produced in the lab the fidelity must be extracted. As shown in [1] this can be done by rewriting the expression for the fidelity as

$$\begin{aligned}
&F = \langle\psi|\rho_{exp}|\psi\rangle = \mathrm{Tr}\left(\rho_{exp} |\psi\rangle\langle\psi|\right) \\
&2 |\psi\rangle\langle\psi| = \hat{P}_z + \hat{\chi} \\
&\hat{P}_z = |0\rangle\langle 0|^{\otimes N} + |1\rangle\langle 1|^{\otimes N} \\
&\hat{\chi} = |0\rangle\langle 1|^{\otimes N} + |1\rangle\langle 0|^{\otimes N} = \frac{1}{N} \sum_{k=0}^{N-1} (-1)^k \hat{M}_k \\
&\hat{M}_k = \left(\cos\left(\frac{\pi k}{N}\right)\hat{\sigma}^x + \sin\left(\frac{\pi k}{N}\right)\hat{\sigma}^y\right)^{\otimes N}.
\end{aligned} \tag{126}$$

The $\hat{P}_z$ operator is measured by measuring all qubits in the z-basis and summing the counts where every qubit was in the $|0\rangle$ or $|1\rangle$ state and dividing by the total number of counts. The $\hat{M}_k$ operator is a measurement of all the qubits in the xy-plane in the basis with an angle $\frac{\pi k}{N}$ relative to the x-axis. This equation can seen to be true by rewriting

$$\hat{M}_k = \left(\exp\left(-i\frac{\pi k}{N}\right)|0\rangle\langle 1| + \exp\left(i\frac{\pi k}{N}\right)|0\rangle\langle 1|\right)^{\otimes N} = \sum_{\epsilon}\exp\left(\frac{\pi k}{N}(N-2n(\epsilon))\right)|\bar{\epsilon}\rangle\langle\epsilon|\,, \tag{127}$$

where ϵ is a sequence of N 0's and 1's and $\bar{\epsilon}$ is the inverse sequence where all 0's are replaced by 1's and vice versa. The sum is over all 2^N possible sequences and $n(\epsilon)$ counts the number of 1's in the sequence. This can all be combined to

$$\begin{aligned}\hat{\chi} &= \frac{1}{N}\sum_{k=0}^{N-1}(-1)^k\sum_{\epsilon}\exp\left(\frac{\pi k}{N}(N-2n(\epsilon))\right)|\bar{\epsilon}\rangle\langle\epsilon| \\ &= \sum_{\epsilon}|\bar{\epsilon}\rangle\langle\epsilon|\,\frac{1}{N}\sum_{k=0}^{N-1}\exp\left(-2\pi k\frac{n(\epsilon)}{N}\right).\end{aligned} \tag{128}$$

Since $2\pi\cdot 0\cdot\frac{n(\epsilon)}{N}$ and $2\pi\cdot N\cdot\frac{n(\epsilon)}{N}$ are both multiples of 2π then the sum over all these exponentials is 0 unless $\frac{n(\epsilon)}{N}$ is an integer in which case the sum gives N. The only way this is possible is if $n(\epsilon)$ is 0 or N which concludes the proof.

6.6.2 Linear cluster state

The protocol for generating a linear cluster state is very similar to that of a GHZ state. The only difference is an extra Hardamard operator between each of the control not operators.

$$\begin{aligned}|\psi_N\rangle &= \prod_{n=1}^{N-1}\hat{H}_0\hat{U}^{cnot}_{0,N-n}\hat{H}_0\,|0\rangle^{\otimes N} \\ &= \prod_{n=1}^{N-1}\hat{H}_n\prod_{n=1}^{N-1}\hat{H}_0\hat{U}^{cz}_{0,N-n}\,|+\rangle^{\otimes N} \\ &= \hat{H}_0\hat{H}_{N-1}\hat{U}^{cz}_{0,N-1}\big(|\psi_{N-1}\rangle\otimes|+\rangle_{N-1}\big).\end{aligned} \tag{129}$$

To show that this is indeed a linear cluster state a proof by induction will be used. For 2 qubits the state is

$$|\psi_2\rangle = \hat{H}_0\hat{H}_1\hat{U}^{cz}_{01}\,|+\rangle^{\otimes 2} = \hat{U}^{cz}_{01}\,|+\rangle^{\otimes 2}\,. \tag{130}$$

Now assume that it is true for N qubits that

$$|\psi_N\rangle = \prod_{n=1}^{N-2}\hat{U}^{cz}_{n,n+1}\hat{U}^{cz}_{0,N-1}\,|+\rangle^{\otimes N}\,. \tag{131}$$

Next it will be shown to be true for N + 1 qubits

$$
\begin{aligned}
|\psi_{N+1}\rangle &= \hat{H}_0\hat{H}_N\hat{U}^{cz}_{0N}|\psi_N\rangle \\
&= \hat{H}_0\hat{H}_N\hat{U}^{cz}_{0N}\prod_{n=1}^{N-2}\hat{U}^{cz}_{n,n+1}\hat{U}^{cz}_{0,N-1}|+\rangle^{\otimes N} \\
&= \prod_{n=1}^{N-2}\hat{U}^{cz}_{n,n+1}\hat{H}_0\hat{H}_N U^{cz}_{0N}\hat{U}^{cz}_{0,N-1}|+\rangle^{\otimes N} \\
&= \prod_{n=1}^{N-2}\hat{U}^{cz}_{n,n+1}\hat{U}^{cz}_{0N}\hat{U}^{cz}_{N,N-1}|+\rangle^{\otimes N} \\
&= \prod_{n=1}^{N-1}\hat{U}^{cz}_{n,n+1}\hat{U}^{cz}_{N0}|+\rangle^{\otimes N},
\end{aligned}
\tag{132}
$$

which concludes the proof.

To evaluate the fidelity of the state generated experimentally a similar approach as for the GHZ state can be used. As described in [35] the density matrix can be rewritten as

$$
\begin{aligned}
|\psi\rangle\langle\psi| &= \prod_{i\in even}\hat{G}_i\prod_{j\in odd}\hat{G}_j \\
\hat{G}_i &= \frac{\hat{I}+\hat{g}_i}{2},
\end{aligned}
\tag{133}
$$

where $\hat{g}_i = \hat{\sigma}^z_{i-1}\hat{\sigma}^x_i\hat{\sigma}^z_{i+1}$ for $i \in [1, N-2]$ and $\hat{g}_0 = \hat{\sigma}^x_0\hat{\sigma}^z_1$ and $\hat{g}_{N-1} = \hat{\sigma}^z_{N-2}\hat{\sigma}^x_{N-1}$. Now measuring the fidelity is as simple as measuring the expectation values of all combinations of $\hat{g}_i$ for which there are 2^N unique combinations. The 3 and 4 qubit cases will be shown here since they are important.

$$
\begin{aligned}
8\,|\psi_3\rangle\langle\psi_3| &= \hat{I}_0\hat{I}_1\hat{I}_2 + \hat{\sigma}^x_0\hat{\sigma}^z_1\hat{I}_2 + \hat{I}_0\hat{\sigma}^z_1\hat{\sigma}^x_2 + \hat{\sigma}^z_0\hat{\sigma}^x_1\hat{\sigma}^z_2 + \hat{\sigma}^z_0\hat{\sigma}^y_1\hat{\sigma}^y_2 + \hat{\sigma}^y_0\hat{\sigma}^y_1\hat{\sigma}^z_2 + \hat{\sigma}^x_0\hat{I}_1\hat{\sigma}^x_2 - \hat{\sigma}^y_0\hat{\sigma}^x_1\hat{\sigma}^y_2 \\
16\,|\psi_4\rangle\langle\psi_4| &= \hat{I}_0\hat{I}_1\hat{I}_2\hat{I}_3 + \hat{\sigma}^x_0\hat{\sigma}^z_1\hat{I}_2\hat{I}_3 + \hat{I}_0\hat{\sigma}^z_1\hat{\sigma}^x_2\hat{\sigma}^z_3 + \hat{\sigma}^z_0\hat{\sigma}^x_1\hat{\sigma}^z_2\hat{I}_3 + \hat{I}_0\hat{I}_1\hat{\sigma}^z_2\hat{\sigma}^x_3 \\
&+ \hat{\sigma}^x_0\hat{I}_1\hat{\sigma}^x_2\hat{\sigma}^z_3 + \hat{\sigma}^y_0\hat{\sigma}^y_1\hat{\sigma}^z_2\hat{I}_3 + \hat{\sigma}^x_0\hat{\sigma}^z_1\hat{\sigma}^z_2\hat{\sigma}^x_3 + \hat{\sigma}^z_0\hat{\sigma}^y_1\hat{\sigma}^y_2\hat{\sigma}^z_3 + \hat{I}_0\hat{\sigma}^z_1\hat{\sigma}^y_2\hat{\sigma}^y_3 + \hat{\sigma}^z_0\hat{\sigma}^x_1\hat{I}_2\hat{\sigma}^x_3 \\
&- \hat{\sigma}^y_0\hat{\sigma}^x_1\hat{\sigma}^y_2\hat{\sigma}^z_3 + \hat{\sigma}^x_0\hat{I}_1\hat{\sigma}^y_2\hat{\sigma}^y_3 + \hat{\sigma}^y_0\hat{\sigma}^y_1\hat{I}_2\hat{\sigma}^x_3 - \hat{\sigma}^z_0\hat{\sigma}^y_1\hat{\sigma}^x_2\hat{\sigma}^y_3 + \hat{\sigma}^y_0\hat{\sigma}^x_1\hat{\sigma}^x_2\hat{\sigma}^y_3.
\end{aligned}
\tag{134}
$$

However, there are two issues with this approach. First the number of terms, and therefor measurements, is exponential in the number of qubits. This makes it infeasible to get the exact fidelity for large states. This can be circumvented by measuring estimates or bounds on the fidelity as shown in [35]. The other issue is that in this system it is not possible to measure different qubits in multiple axes in the xy-plane in a single measurement. This means that the last operator for the 3-qubit case and the last 5 operators for the 4-qubit case cannot be measured physically.

6.7 Physical state generation

In the following discussion the protocol for generating these states in the physical system will be discussed. Qubit 0 is the spin of the electron trapped within the QD. Any χ-rotation on this spin can be achieved using

Raman pulses thereby allowing any single qubit operation. All of the other qubits will be time-bin encoded photons.

There are $N-1$ photon packets each consisting of an early (e) and late (l) pulse. The qubit information will be encoded in whether the photon is located in the early or late pulse corresponding to the z-basis. The xy-basis depends on the phases between the early and late pulses. The operation of generating a photon in pulse p (e/l) of packet n if the spin is in state $|1\rangle$ is given by $\hat{U}^e_{0,pn}$. Upon finishing the protocol each packet can be collapsed to a single qubit by applying the operator

$$\hat{C}_n = (a_0 |0\rangle_n + b_0 |1\rangle_n) \langle 10|_{en,ln} + (a_1 |0\rangle_n + b_1 |1\rangle_n) \langle 01|_{en,ln} , \tag{135}$$

where the values of a_i and b_i determine the interpretation of the photons. It must be true that $|a_i|^2 + |b_i|^2 = 1$ and $a_0^* a_1 + b_0^* b_1 = 0$. The collapse operator is not an actual operator which is performed on the state but a mathematical construct to encode the interpretation of the photonic pulse qubits.

In this work the control not operator is performed by applying $\hat{R}^y(\pi)\hat{U}^e_{ln}\hat{R}^y(\pi)\hat{U}^e_{en}$ and the late photon is interpreted as the $|0\rangle$ state yielding $\hat{C}_n = |0\rangle_n \langle 01|_{en,ln} + |1\rangle_n \langle 10|_{en,ln}$. From straight forward calculations applying this sequence on an arbitrary spin state yields

$$\hat{C}_n \hat{R}^y(\pi)\hat{U}^e_{ln}\hat{R}^y(\pi)\hat{U}^e_{en}(A |0\rangle_0 + B |1\rangle_0) |00\rangle_{en,ln} = -A |00\rangle_{0n} - B |11\rangle_{0n} , \tag{136}$$

which shows that $\hat{R}^y(\pi)\hat{U}^e_{ln}\hat{R}^y(\pi)\hat{U}^e_{en} = \hat{U}^{cnot}_{0n}$ up to a global factor -1. This protocol can be seen in figure 9

6.7.1 GHZ state

The GHZ state protocol is quite simple now. After initializing the spin to $|0\rangle$ a $\hat{R}^y\left(\frac{\pi}{2}\right)$ operation is perform to rotate it into the $|+\rangle$ state just like a Hardamard operator would. Then the $\hat{R}^y(\pi)\hat{U}^e_{ln}\hat{R}^y(\pi)\hat{U}^e_{en}$ sequence is performed for all photon packets. After this the GHZ state has been generated up to a global phase.

However, there is another protocol which requires fewer rotations. For an even number of photon packets the last pi-rotation in each photon generation sequence is omitted, thus the photon generation sequence is $\hat{U}^e_{ln}\hat{R}^y(\pi)\hat{U}^e_{en}$. Upon performing this on two consecutive packets the result is $-A |00110\rangle_{0,e2n-1,l2n-1,e2n,l2n} - B |11001\rangle_{0,e2n-1,l2n-1,e2n,l2n}$ and thus this is once again control not operations up to a global factor if for every second photon packet the first photon is interpreted as the $|0\rangle$ state. This means the collapse operators are $\hat{C}_{2n-1} = |0\rangle_{2n-1} \langle 01|_{2n-1} + |1\rangle_{2n-1} \langle 10|_{2n-1}$ and $\hat{C}_{2n} = |0\rangle_{2n} \langle 10|_{2n} + |1\rangle_{2n} \langle 01|_{2n}$. For an odd number of photon packets it is the same protocol except for an extra pi-rotation at the end.

6.7.2 Linear cluster state

The linear cluster state generation is also very similar. For this protocol the last pi-rotation in the photon generation protocol is switched for a negative pi/2-rotation instead, then the protocol is $\hat{R}^y\left(-\frac{\pi}{2}\right)\hat{U}^e_{ln}\hat{R}^y(\pi)\hat{U}^e_{en}$.

The collapse operator is also changed to include a pi-phase on the early photon $\hat{C}_n = |0\rangle_n \langle 01|_{en,ln} - |1\rangle_n \langle 10|_{en,ln}$.

7 Error modelling

In this section the generation of a GHZ and linear cluster state, and performance of Deutsch's algorithm in these, will be modelled using a Monte Carlo simulation. A number of error sources will be described and implemented as well to account for the infidelities. Using this simulation the fidelity of the states that can be generated with this system will be estimated along with the fidelity of Deutsch's algorithm implemented within these states.

7.1 Ideal model

First the ideal model without any errors will be described. A set of early/late pulses will be called a photonic qubit. The total Hilbert space of the system is the 4-level system of the spin combined with the number states for each pulse. The first approximation will be to remove the exciton states. Since these will always decay, any excitation to a trion state can just be modelled as a rotation to the state to which it will decay. All the pulses will also be truncated at 2 photons such that the total Hilbert space is 2-dimensional for the spin state and 3x3 dimensional for each photonic qubit for a total size of

$$D_{raw} = 2 \cdot 9^{N-1}, \tag{137}$$

where N is the number of qubits. A state will be written as $|n_0 n_1 ... n_{N-1}\rangle$ or as $|n_0\rangle |n_1\rangle ... |n_{N-1}\rangle$ where n_0 referrers to the spin state and the n_i for $i > 0$ referrers to the ith photonic state. The annihilation operators for the photon pulses will be $\hat{a}_n^m = |0\rangle\langle 1|_{pn} + |1\rangle\langle 2|_{pn}$ for qubit n and p can be e/0 for early or l/1 for late. In the end the photonic states will be converted into qubits using early/late encoding.

To start the simulation a state is prepared in the $|0\rangle^{\otimes N}$ state as the ideal preparation. After this a series of operators can be applied. One of the possible operators is a rotation operator which can be applied to the spin to rotate it around any axis in the xy-plane given by equation 88

$$\hat{R}^{\chi}(\theta) = \cos\left(\frac{\theta}{2}\right)(|0\rangle\langle 0|_0 + |1\rangle\langle 1|_0) - i\sin\left(\frac{\theta}{2}\right)(\exp(-i\chi)|0\rangle\langle 1|_0 + \exp(i\chi)|1\rangle\langle 0|_0). \tag{138}$$

Next an excitation operator can also be applied which will create a photon in a pulse if the spin is in state $|1\rangle$ given by

$$\hat{E}_n^p = \hat{I}_n^p |0\rangle\langle 0| + (\hat{a}_n^p)^{\dagger} |1\rangle\langle 1|. \tag{139}$$

7.2 Losses

The probability to loose a photon between the dot and the interferometer is $1 - \tilde{\epsilon}$ and thus when applying an excitation operator a collapse operator $\frac{|1\rangle\langle 1|}{|\langle 1|\psi\rangle|}$ will instead be applied with probability $p = (1 - \tilde{\epsilon})|\langle 1|\psi\rangle|^2$ where $|\psi\rangle$ is the state before the operator. The rest of the time the normal excitation operator will be applied.

$$\hat{E}_n^p = \frac{\hat{I}_n^p \left|0\right\rangle\!\left\langle 0\right| + \sqrt{\tilde{\epsilon}}(\hat{a}_n^p)^\dagger \left|1\right\rangle\!\left\langle 1\right|}{\sqrt{\left|\langle 0|\psi\rangle\right|^2 + \tilde{\epsilon}\left|\langle 1|\psi\rangle\right|^2}}. \tag{140}$$

The collapse operator models a photon being created and then absorbed before it reached the interferometer and was able to interfere with anything. After applying all of the operators the state is discarded if more than two photons were generated within one qubit, this means applying the operator $\left|00\right\rangle\!\left\langle 00\right|_{el} + \left|10\right\rangle\!\left\langle 10\right|_{el} + \left|01\right\rangle\!\left\langle 01\right|_{el} + \left|20\right\rangle\!\left\langle 20\right|_{el} + \left|02\right\rangle\!\left\langle 02\right|_{el} + \left|11\right\rangle\!\left\langle 11\right|_{el}$ for each photonic qubit. This is done because generating more than two photons is very unlikely and it saves a lot of computational power during the measurement phase. This process is repeated a number of times and a mixed state is generated by averaging all of the pure states generated this way.

7.3 Measurement

After the mixed state is generated all the qubits are measured. This is done by projecting the generated state onto each of the possible states which can be measured. The spin can only be measured when it is in the $|1\rangle$ state so to measure the $|0\rangle$ state an extra pi-rotation must be applied and then measure the state again. Any state which did not yield the spin state of $|1\rangle$ will be discarded as is done in the lab. When the spin is in the $|1\rangle$ state it will be discarded with a probability of F_n and when it is in the state $|0\rangle$ it will be kept with probability of F_p.

Each photonic qubit can either be measured in the z-basis by measuring it in the early or late pulse or in the χ-basis in the xy-plane by interfering the early and late pulse with an added phase of χ on the early pulse. The loss from the interferometer to the detector and the detector inefficiency is combined into a total inefficiency of $1-\epsilon$. All combination of projections are performed such that if there are two photonic qubits and they are measured in the x-basis and the z-basis respectively the 4 projections would be $|0\rangle\,|+\rangle$, $|0\rangle\,|-\rangle$, $|1\rangle\,|+\rangle$ and $|1\rangle\,|-\rangle$ on top of the spin projection.

If a z-measurement is performed the possible projections for detecting a photon are $\sqrt{1-F_d}\,|0\rangle\ \sqrt{\epsilon}\,|1\rangle$, $\sqrt{1-(1-\epsilon)^2}\,|2\rangle$. The projections for detecting no photons are $\sqrt{F_d}\,|0\rangle\ \sqrt{1-\epsilon}\,|1\rangle$, $(1-\epsilon)\,|2\rangle$. The prefactors take into account the losses and dark counts/background photons of the detector. Each of the cases counts as measuring a photon. This is done for both pulses in the qubit.

On the other hand if a χ-measurement is done the effect of the interferometer has to be applied first. The interferometer adds the phase χ to the early photon and then interferes the early and later photon on a beam splitter. This is done by transforming the density operator as

$$
\begin{aligned}
&\hat{\rho} \to \hat{U}(\chi)\hat{\rho}\hat{U}^{\dagger}(\chi) \\
&\hat{U}(\chi) = |00\rangle_{01}\langle 00|_{el} + \frac{i\exp(i\chi)}{\sqrt{2}}(|10\rangle_{01} + i\,|01\rangle_{01})\langle 10|_{el} + \frac{1}{\sqrt{2}}(|01\rangle_{01} + i\,|10\rangle_{01})\langle 01|_{el} \\
&- \frac{\exp(2i\chi)}{2}\Big(|20\rangle_{01} - |02\rangle_{01} + i\sqrt{2}\,|11\rangle\Big)\langle 20|_{el} + \frac{1}{2}\Big(|02\rangle_{01} - |20\rangle_{01} + i\sqrt{2}\,|11\rangle\Big)\langle 02|_{el} \\
&+ \frac{i\exp(i\chi)}{2}\Big(i\sqrt{2}\,|20\rangle_{01} + i\sqrt{2}\,|02\rangle_{01}\Big)\langle 11|_{el}
\end{aligned}
\tag{141}
$$

This will transform the $\frac{1}{\sqrt{2}}(|10\rangle_{el} \pm \exp(i\chi)\,|01\rangle_{el})$ into $|10\rangle_{01}$ for plus and $|01\rangle_{01}$ for minus. Then the z-measurement protocol is applied.

7.4 Initalization

When initializing the state all photon states are initialized to 0 photons with fidelity of 1. However, the spin may not be initialized correctly. Since it is initialized using decays it may decay to the correct spin state or to the wrong state. This can be modelled by simply using the initial spin state of $|0\rangle$ with probability F_I and spin state $|1\rangle$ with probability $1 - F_I$.

7.5 Rotation Errors

The next place an error could occur is during rotation of the spin. The first type of possible error is an incoherent spin flip. An incoherent spin flip may occur due to a decay during the rotation pulse or through other mechanics like kicking out the electron and allowing a new one to tunnel into the dot. But all these effects can be described the same way. If a rotation pulse of duration T is applied and there is an incoherent spin flip rate of τ then first a time t is sampled from the exponential distribution

$$
P(t) = \frac{1}{\tau}\exp\left(-\frac{t}{\tau}\right), \tag{142}
$$

this will be the time for the next spin flip. If $T \leq t$ then the rotation is just applied and no spin flip occurs. If $T > t$ then a rotation of duration t is applied followed by a spin flip operator which is chosen from one of the following

$$
\begin{aligned}
\hat{S}_{00} &= |0\rangle\langle 0| \\
\hat{S}_{01} &= |0\rangle\langle 1| \\
\hat{S}_{10} &= |1\rangle\langle 0| \\
\hat{S}_{11} &= |1\rangle\langle 1|\,,
\end{aligned}
\tag{143}
$$

with operator $\hat{S}_{ij}$ with probability $|\langle j|\psi\rangle|^2$. After this the process is repeated with T replaced by $T - t$.

Secondly it is assumed that the duration of a rotation operation has been calibrated such that the average duration is correct, however, short time fluctuations in the rotation power cannot be corrected for and may still

occur. It will be assumed that the error of the power follows a normal distribution and the rotation duration is proportional to the square root of the power. Therefor if the correct duration is T_r then the actual duration applied will be $T = \sqrt{1 + E_r}T_r$ where E_r is a random number sampled from a normal distribution with mean of 0 and standard deviation of σ_r.

Finally due to coupling to the nuclear spin environment the energy splitting between spin up and spin down may change randomly. This will cause a detuning in the rotation of Δ_r which will be sampled from a normal distribution with mean 0 and standard deviation δ_r.

7.6 Spin Decoherence

The spin can also decohere. This is not associated with any operator but is an effect that occurs constantly. It will be assumed that all operators are very fast compared to the decoherence time such that it can be assumed that no decoherence occurs during operations. As described in section 2.3.3 this is caused by the nuclear spin environment and will cause an effective z-rotation of the spin. It will be assumed that during a very short time scale the spin will rotate by some constant amount which is constant for all times and some random amount which is random every time step. This means that during this very short time scale Δt the spin will experience the rotation $R^z(\phi_l \Delta t + \epsilon)$, where ϕ_l is a constant and ϵ is a random number from some distribution with mean 0 and standard deviation σ_d. Thus over a long time period t this will add up to $R^z(\phi_l t + \sum_i \epsilon_i)$ where ϵ_i are all the random contributions. The distribution of this random variable does not matter since the sum will follow the central limit theorem and the random contribution can be replaced by one random variable ϵ_d sampled from a normal distribution with mean 0 and variance $\sigma_d^2 t$ yielding the total rotation of $R^z(\phi_l t + \epsilon_d)$. This rotation will be applied to the spin between every operator where t is the time between applying the operators.

7.7 Spin Flip Errors

Very similar to the spin decoherence is the passive spin flip rate of τ_s which is a T_1 error. The electron will randomly flip its spin over long time scales due to interactions with the electronic environment. Just like decoherence this is implemented as an operation that can occur between other operators. If one operator is applied at time t_0 and the next is applied at time $t_0 + T$ then if a random number $t < T$ for t drawn from the distribution $\frac{1}{\tau_s} \exp\left\{-\frac{t}{\tau_s}\right\}$ one of the spin flip operators will be applied.

7.8 Excitation Errors

The final place an error could occur is during the excitation operation. This is the operation where the most things can go wrong and thus it is the most complicated operator. First, just like for the rotation pulse the average duration of the excitation rotation is assumed to be correct but each time the operator is applied there may be some random error such that the applied duration is $T = \sqrt{1 + E_e}T_e$ where T_e is the correct duration and E_e is a random number with mean 0 and standard deviation σ_e. Also just like for the rotation operation there may be some random detuning Δ_e sampled from a normal distribution with mean Δ_e^0 and standard de-

viation δ_e where Δ_e^0 can be set in the experiment.

Due to the width of the excitation laser pulse and the finite lifetime of the quantum dot there is also a finite probability to do a double excitation where two photons are generated within the same pulse. This probability P_{pd} is calculated from the simulation described in section 3.7 from a FWHM of the pulse of Δ_p and a lifetime of γ. On top of this an intrinsic probability of P_d to generate two photons is added. Another related error is the ability of the system to generate a photon when the spin is in the wrong state. The probability of this occuring is P_w and is given by the same simulation when detuned by the detuning of the cycling transitions denoted by Δ. If a wrong photon is generated it will have a wrong frequency leading to the loss of the photon during filtering which collapses the state. This is implemented by applying the operator $\frac{|0\rangle\langle 0|}{|\langle 0|\psi\rangle|}$ with probability P_w or the operator $\frac{|1\rangle\langle 1|+\sqrt{1-P_w}|\langle 0|\psi\rangle||0\rangle\langle 0|}{\sqrt{|\langle 1|\psi\rangle|^2+(1-P_w)|\langle 0|\psi\rangle|^2}}$ with probability $1-P_w$.

Finally a number of errors will lead to the photon being lost, this could be a decay into a radiative mode, loss of a photon or a phonon sideband decay or a non-cycling decay which will generate a photon of a wrong frequency which is then filtered away. All of these cases are combined into the efficiency $\tilde{\epsilon}$ with $\tilde{\epsilon} = \tilde{\epsilon'} + \frac{C}{C+1}$.

7.9 Simulation Results

All of the parameters was estimated, and shown in table 1, to the best of our ability, however, some parameters like the laser power and detuning fluctuations were difficult to estimate and was mostly guessed. Therefor, the results of the simulation will not be exactly like the real experiment. Some errors were also not implemented, one of these errors was the indistinquishability of the photons since this would increase the size of the Hilbert space a lot and would slow down the program. There are probably also others errors which has not been considered. Each of the simulations is done by generating 160000 states in a Monte Carlo simulation the states were used to calculate the density matrix from which all results were evaluated.

The results of the simulation are shown in table 2. The fidelity of the generated state is shown along with the contributions from the z-basis and the xy-basis. The fidelities of the 3-qubit Deutsch's algorithm is also shown. 3 different cases are simulated. First is the state which was generated in the experiment, second is the modified GHZ generation protocol with only a single pi-rotation per photonic qubit. Finally there is the same protocol as in the experiment but with the detuning between the two cycling transitions set to 30 GHz. This corresponds to using the direct transitions as the cycling transitions which would be true if the waveguide had been manufactured along the correct axis. The pulse width of the excitation pulse was scanned in the simulation and the best width of 20 ps is shown here.

This result can be compared to the results from the experiment shown in table 6. The fidelity of the simulation is very similar to that of the experiment, however, the contributions are split differently. In the simulation $\left\langle \hat{P}_z \right\rangle$ is considerably higher than in the experiment while $\langle \hat{\chi} \rangle$ is lower. Since the z-fidelity is mainly determined by the spin flip processes and rotation fidelity it is likely that one of these processes has been underestimated. The

Parameter	Value
$\tilde{\epsilon'}$	0.15
ϵ	1 / 15
F_d	0.9999
F_n	0.88
F_p	0.01
F_I	0.99
ϕ_l	1 / 33 ns^{-1}
σ_d	$\sqrt{2/600}$ ns^{-1}
τ	1 / 30 T_π^{-1}
τ_s	1 / 1000 ns^{-1}
σ_r	0.02
δ_r	0.05 GHz
σ_e	0.02
δ_e	0.02 GHz
Δ_e^0	0 GHz
Δ_p	30 ps
γ	1 / 200 ps^{-1}
Δ	10 GHz
P_d	0.01
C	30

Table 1: *A list of all the parameter values used in the simulation. T_π is the pi-rotation time.*

Measure	GHZ state	GHZ state no middle pi-pulse	GHZ state with $\Delta = 30, \Delta_p = 20$
$\left\langle \hat{P}_z \right\rangle$	0.814 ± 0.004	0.834 ± 0.004	0.819 ± 0.003
$\langle \hat{\chi} \rangle$	0.253 ± 0.002	0.255 ± 0.002	0.505 ± 0.002
F	0.533 ± 0.002	0.545 ± 0.002	0.662 ± 0.002
F_c	0.888 ± 0.002	0.893 ± 0.002	0.891 ± 0.002
F_b	0.910 ± 0.003	0.927 ± 0.003	0.913 ± 0.002

Table 2: *The results of the simulation of the GHZ state generation, the fidelity of the state is related to the expectation values by $F = \frac{\left\langle \hat{P}_z \right\rangle + \langle \chi \rangle}{2}$. F_c (F_b) are the fidelities for the constant (balanced) case of the 3 qubit implementation of Deutsch's algorithm. The GHZ state is using the normal GHZ state generation protocol. GHZ state no middle pi-pulse is using the modified GHZ state generation protocol with only one pi-pulse per photonic qubit. GHZ state with $\Delta = 30, \Delta_p = 20$ is the normal GHZ state generation protocol with the value for Δ if the wafer had been manufactured correctly. The width of the MIRA pulse is set to the optimal value of 20 ps.*

xy-fidelity is more sensitive to the decoherence of the spin which means the decoherence effects may have been overestimated. However, the simulation is still close to the experiment and useful to see what can be done to improve the results.

From column two it is seen that optimized GHZ generation protocol can improve the fidelity a bit. It has the biggest effect on the z-fidelity since the rotation pulses mainly introduce spin flips and rotation errors. This also results in a bit better quantum algorithm fidelities since these are closely related to the z-fidelity. Although the effect is small the protocol is still preferable since it is more simple to implement and there is no downside.

The biggest improvement is with a larger cycling transition detuning. This improves the fidelity by 13 %. It is observed that the entire improvement is in the xy-fidelity which is as expected since the detuning error causes dephasing which does not affect the z-fidelity. Therefor, the algorithm fidelities are also not affected either. This shows that changing to a sample which has been manufactured in the correct orientation could improve the fidelity by a lot and possibly allow for 3 or 4 photon states with decent fidelity.

The simulation was also run with $\Delta_p = 7.5GHz$ to attempt to increase the fidelity as predicted in figure 5. However, surprisingly the fidelity dropped during this simulation so this does not seem like a good idea from the simulation. This result is not understood and perhaps a bug in the simulation caused this.

Finally the error contributions from all the parameters were estimated in table 3. This was done by running the simulation with realistic values for all parameters yielding a fidelity of F_0. The error contribution was estimated by removing the parameter p from the simulation and simulating with all the other parameters at the same values yielding the fidelity F_p. The error was calculated as $1 - \frac{F_0}{F_p}$. This assumes that all errors are decoupled which is not true but it gives a good measure for how well the system can be improved by improving individual errors. This is useful for focusing the optimization effort. The results show that the z-fidelity is indeed mostly affected by rotation errors and spin flips and the xy-fidelity is mostly affected by dephasing errors. Especially the error from generating photons when the spin is in the wrong state is very large. Other large errors are the spin readout fidelities and the incoherent spin flips. This shows that focusing on these problems could improve the system the most.

The prospects for generating more advanced states were also explored by simulating both a 3-qubit and a 4-qubit linear cluster state using the errors with a wafer manufactured in the correct orientation. These results are shown in figure 4. The results show that the cluster state does have a lower fidelity than the GHZ state. This is most likely because the cluster state generation keeps mixing the z-basis and x-basis, this makes it more sensitive to dephasing errors than the GHZ state. It also shows an 8 % decrease in fidelity by adding a photon to the cluster state which would have a fidelity of around 50 %. This means a 4-qubit experiment is very possible with a new wafer, however, 5 qubits or more may start having to low fidelities. 5 or more qubits also cannot be done until the collection efficiency is improved a lot since it would take forever to get any data.

Parameter	F	$\left\langle \hat{P}_z \right\rangle$	$\langle \hat{\chi} \rangle$
P_w	0.175 ± 0.004	0.005 ± 0.005	0.467 ± 0.006
F_p	0.098 ± 0.005	0.077 ± 0.006	0.158 ± 0.010
F_n	0.091 ± 0.005	0.074 ± 0.006	0.141 ± 0.012
τ	0.065 ± 0.005	0.048 ± 0.005	0.114 ± 0.012
P_{pd}	0.030 ± 0.007	-0.002 ± 0.007	0.120 ± 0.011
ϵ	0.030 ± 0.005	0.023 ± 0.005	0.055 ± 0.009
δ_r	0.029 ± 0.006	0.030 ± 0.006	0.022 ± 0.014
$\tilde{\epsilon'}$	0.028 ± 0.006	0.017 ± 0.007	0.058 ± 0.013
τ_s	0.025 ± 0.006	0.018 ± 0.005	0.044 ± 0.012
C	0.023 ± 0.006	0.015 ± 0.006	0.047 ± 0.010
F_d	0.023 ± 0.006	0.020 ± 0.006	0.027 ± 0.014
σ_d	0.021 ± 0.006	0.005 ± 0.006	0.067 ± 0.012
F_I	0.018 ± 0.005	0.011 ± 0.005	0.037 ± 0.010
σ_r	0.014 ± 0.006	0 ± 0.007	0.003 ± 0.014
σ_e	0.014 ± 0.006	0.010 ± 0.007	0.024 ± 0.016
δ_e	0.012 ± 0.005	0.011 ± 0.006	0.013 ± 0.012
P_d	0.006 ± 0.007	-0.003 ± 0.007	0.031 ± 0.013
ϕ_l	0.003 ± 0.007	-0.003 ± 0.007	0.021 ± 0.016

Table 3: *The error contributions of each of the parameters. First the simulation is run with realistic values for all parameters yielding a fidelity of F_0. The error contribution has been estimated by removing the parameter p from the simulation and simulating with all the other parameters at the same values yielding the fidelity F_p. The error is calculated as $1 - \frac{F_0}{F_p}$.*

State	Fidelity	Uncertainty
3-qubit GHZ	0.662	0.002
3-qubit cluster state	0.557	0.002
4-qubit cluster state	0.481	0.004

Table 4: *Fidelity of states generated with the wafer manufactured correctly. The cluster states have lower fidelity than the GHZ state and more than 4 qubits starts to have very low fidelity.*

Algorithm	Constant	Balanced
3-qubit Deutsch's algorithm	0.890 ± 0.002	0.768 ± 0.003
4-qubit constant/balanced	0.888 ± 0.005	0.759 ± 0.007
4-qubit $f(0)$	0.847 ± 0.006	0.647 ± 0.005

Table 5: *Fidelity of different versions of Deutsch's algorithm in cluster states. Both the constant and balanced functions are shown. The three cases are the 3-qubit version, the 4-qubit version to measure constant/balanced and the 4-qubit version to measure $f(0)$. The 3-qubit and 4-qubit versions have almost the same fidelity, however, determining $f(0)$ has lower fidelity.*

Deutsch's algorithm has also been simulated within the cluster states, this is shown in figure 5. The results show that the 3-qubit version of the algorithm can be done fairly well. Since the algorithm no longer just requires z-basis measurements, the fidelity is lower than in the GHZ state for the balanced case while the constant case is approximately the same. It can also be seen that the 4-qubit version of the algorithm is almost as good as the 3-qubit version, however, when measuring $f(0)$ of the 4-qubit version the fidelity is considerably lower.

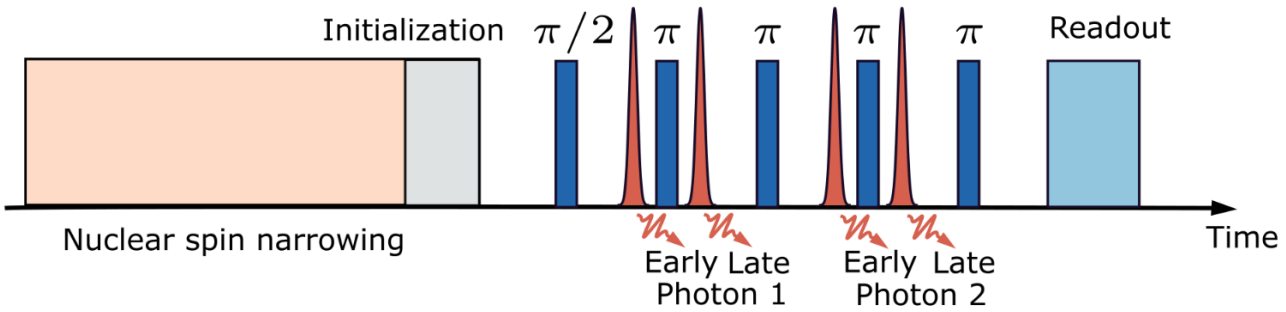

Figure 9: *The entire protocol for generating a GHZ state. It starts with a nuclear spin narrowing and an initialization pulse. Then comes $N-1$ short sequences of MIRA pulse, pi-rotation, MIRA pulse, pi-rotation for an N photon GHZ state, finally there is a readout pulse to check if the spin is down. The sequence may also be modified by changing the last rotation to measure a different spin state. The figure has been made by Yijian Meng*

8 Experimental results

8.1 Protocol

The final protocol for generating GHZ states is a three step process as show in figure 9. First there is the initialization step. It starts with a long period of nuclear spin narrowing which lasts for 1 μs. This is followed by the initialization pulse which is active for 100 ns. The second step is the photon generation. Here the sequence of MIRA-pulse, pi-rotation, MIRA-pulse, pi-rotation is repeated $N-1$ times for the N qubit GHZ state, in this work that is twice. The last step is the readout step where the readout pulse is applied for 100 ns. The total duration is 1.8 μs. If no photons or more than one photon is detected within any packet of photons the state is discarded. Since there is high loss receiving no photons during the readout pulse does not imply a spin up so it is only possible to measure spin down. If no photons are received then the state is discarded, this causes the rate to be halved. This is repeated a lot of times and the resulting data is a 2^{N-1} array of data, in this case 2x2. The n'th dimension of this array is the result of the measurement of photon n and each entry holds the number of successful runs with the given measurement result. Finally to measure the opposite spin state the same experiment is run again the same number of times but with the pi-rotation at the end removed. This allows for the opposite spin state to be measured and the two arrays are combined into a total array of size 2^N. The experiment is repeated $2N$ times after this to measure the xy-projections of the spin state. In these repeats the last pi-rotation replaced with a pi/2-rotation which varies in rotation axis. To measure the spin along the χ axis the rotation axes of $\frac{3}{2}\pi - \chi$ and $\frac{1}{2}\pi - \chi$ are used.

At the point of writing this thesis the active switching has not been implemented yet. This means that it is possible to choose the measurement axis in the xy-plane, but the choice of measuring along the z-axis or along the chosen xy-axis is random. This can be seen in figure 10 where each photon packet consists of three pulses. The first is the early photon going through the short arm of the interferometer, this corresponds to measure the photon in the early bin. The last pulse is the late photon going through the long arm corresponding to a late photon measurement. The middle pulse is both the early photon through the long arm and the late photon

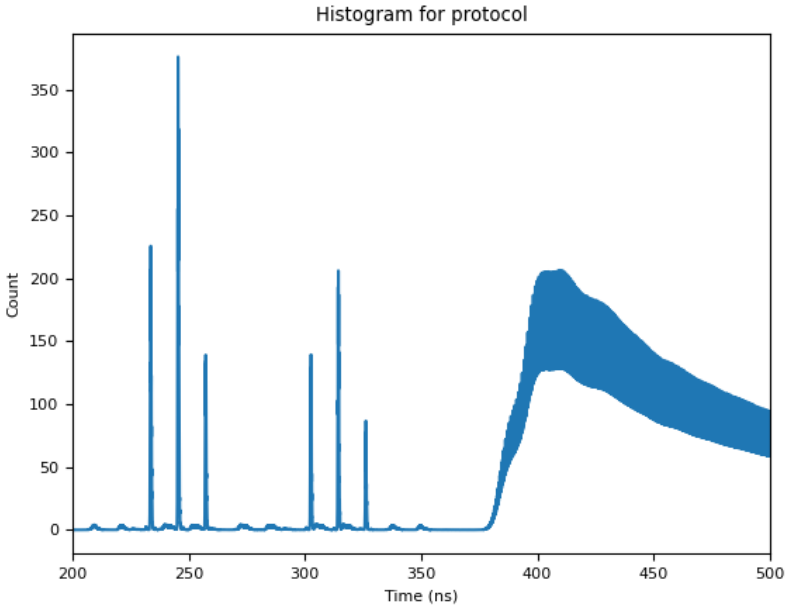

Figure 10: *An example histogram of photon generation and readout step. The three pulses per photon packet are the early photon going through the early arm, the combination of the early photon through the long arm and the late photon through the short arm, and finally the late photon through the long arm.*

through the short arm, these will interfere and the xy-basis measurement is done by seeing what detector receives the photon. Since there is an equal chance to measure in the z-basis and the xy-basis the middle bin contains the same number of photons as the combination of the early and late bins. The discrepency in the number of photons in the early and late bins is because the interferometer is not entirely balanced.

8.2 Results

The results for the fidelity measurement of the 3 qubit GHZ state is shown in figure 11 and is the result of 7470 accepted state generations which were generated at a frequency of 0.13 Hz. The final results for the fidelity is given in table 6 with the total fidelity of $F = 0.56 \pm 0.02$.

Finally the data was also used to evaluate the fidelity of the three qubit Deutsch's algorithm. The fidelity of the constant case was $F_c = 0.88 \pm 0.02$ and the fidelity for the balanced case was $F_b = 0.85 \pm 0.01$. The fidelity for the algorithm is rather high when considering the state fidelity of $F = 0.56 \pm 0.02$. However, this is to be expected since the algorithm only requires z-basis measurements and the z-fidelity is 0.76. If a wrong state is generated the algorithm will essentially just do a random guess thus yielding an extra 0.12 fidelity from random chance. The total expected fidelity would be roughly 0.88 which is what is observed. This also shows that this result is not representative for a general algorithm implementation since the fidelity would drop drastically if any xy-measurement would be required.

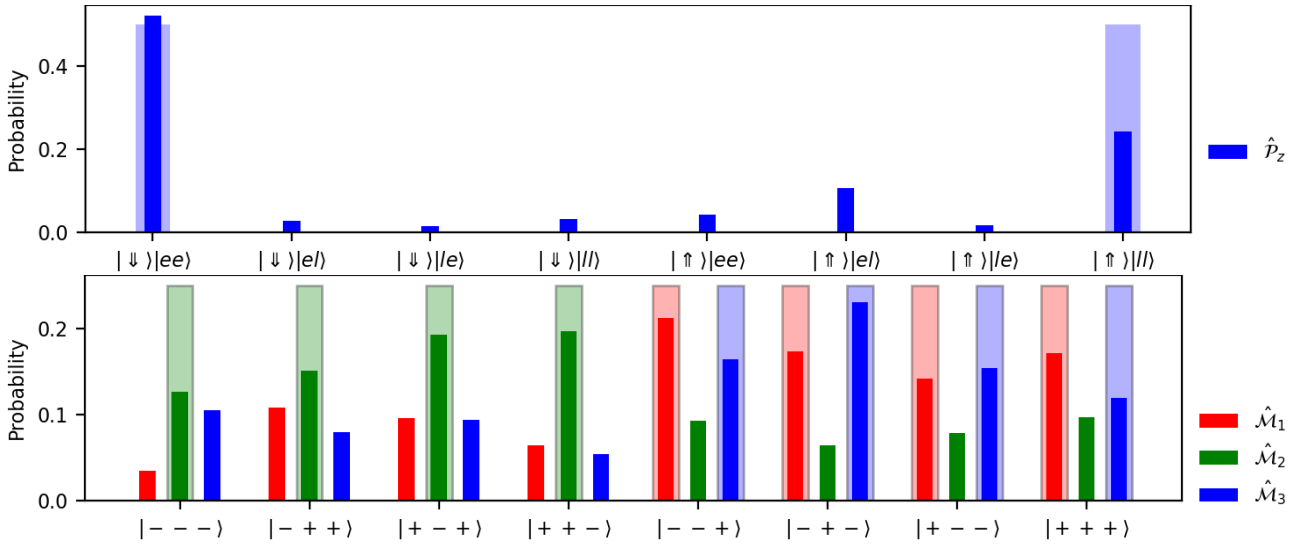

Figure 11: *The results for the fidelity measurement. The shaded regions are the optimal case if pure GHZ states could be generated.* ***top)*** *The results for the z-fidelity, the bar over each state along the x-axis represents the fraction of the measurement results which were in that state.* ***bottom)*** *The results for the xy-fidelity measurement. The +/- states are the positive or negative result along the measurement axis used in the experiment, for $\hat{M}_k$ the axis is $\frac{\pi k}{3}$ relative to the x-axis. For even k there must be an even number of + states and for odd k the number of + states must be odd. The figures are created by Yijian Meng.*

Operator	Expectation Value	Standard Deviation
$\langle \hat{P}_z \rangle$	0.76	0.02
$\langle \hat{M}_1 \rangle$	−0.40	0.05
$\langle \hat{M}_2 \rangle$	0.34	0.04
$\langle \hat{M}_3 \rangle$	−0.34	0.04
F	0.56	0.02
F_c	0.88	0.02
F_b	0.85	0.01

Table 6: *The results of the fidelity measurement of the 3 qubit GHZ state. The total number of measurements used was 7470. The total fidelity is calculated from $F = \frac{\langle \hat{P}_z \rangle + \frac{1}{3}(-\langle \hat{M}_1 \rangle + \langle \hat{M}_2 \rangle - \langle \hat{M}_3 \rangle)}{2}$. F_c (F_b) are the fidelities for the constant (balanced) case of the 3 qubit implementation of Deutsch's algorithm.*

9 Conclusion

The main focus of this thesis has been to generate a 3-qubit GHZ state, consisting of two time-bin encoded photons and one electron spin, and encode Deutsch's algorithm within this state. The work has also focused on understanding the system and error sources to be able to estimate the ability to produce larger states.

The theory behind each of the spin control mechanics and the photon generation protocol has been investigated. From this it was found that errors due to the 4-level spin system during initialization and detection should be very small showing that the limiting factors are background signal or other effects not considered. It was also shown that a Raman pulse could be used to rotate the spin state, with very low error, for full spin control. However, other effects like incoherent spin flips and control of the rotation power currently limits our ability to control the spin. The nuclear spin noise was also investigated, showing that using a spin-echo sequence and nuclear spin cooling could decrease this noise a lot. From experiment it was found that nuclear spin cooling could decrease the noise by a factor 10 for $T_2^* \approx 30ns$ and the spin-echo sequence allows for experiments that lasts for hundreds of nanoseconds. Finally the simulation of the photon generation, assuming Gaussian pulse shapes, showed large g^2 contributions and a poor ability to produce photons conditioned on a specific spin state. However, it was also shown that these effects could be lowered a lot by changing to a new sample since the current sample had a manufacturing error.

The theory of measurement based quantum algorithms was also introduced. The GHZ and linear cluster states were introduced along with protocols for producing the states in our setup. A 5-qubit implementation of Deutsch's algorithm for a linear cluster state was also investigated along with the ability to shorten it to 3 qubits. However, this algorithm was shown to not realize any quantum advantage since a product state could also solve the problem in a single function call. This was solved by allowing the oracle to decide if the experimentalist should determine if $f(0) = f(1)$ or determine the value of $f(0)$ which could only be done with an entangled state. However, this requires a 4-qubit linear cluster state.

The GHZ generation protocol was implemented in the lab yielding a state fidelity of 0.56 ± 0.02 with a z-fidelity of 0.76 ± 0.02 and a xy-fidelity of 0.36 ± 0.04. This show that the xy-fidelity and therefor the dephasing errors are the limiting factors. It was also found that Deutsch's algorithm could be implemented with a fidelity of 0.88 ± 0.02 (0.85 ± 0.01) for the constant (balanced) algorithms. The reason for the large fidelities is that the algorithm only requires z-basis measurements which has a much higher fidelity than the xy-basis measurements.

The experimental system was also simulated using a Monte Carlo simulation to be able to investigate the various error contributions. In this simulation a fidelity of 0.53 was found with a z-fidelity of 0.81 and a xy-fidelity of 0.25 showing that the simulation is fairly accurate but the z-fidelity is overestimated while the xy-fidelity is underestimated showing that some dephasing errors are less severe than believed while some rotation or spin flip errors are worse. It was also found that the largest contribution to the error came from the wrong man-

ufacturing while the spin readout fidelity and the incoherent spin flips are also large contributors. Fixing the sample showed an improved fidelity of 0.66 while the 3- and 4-qubit cluster states have lower fidelities of 0.56 and 0.48. This is due to the cluster state being more prone to dephasing errors.

Finally a simulation approach to optimizing PID values was investigated. The results were promising as only one day of system characterization was needed to run an accurate simulation yielding PID parameter values close to the once optimized by hand over the cause of several weeks. The main reason for the slow optimization by hand is the large input delay of 2 minutes of the PID making evaluation of PID parameter values very slow. The most time consuming part of the characterization script was the ambient temperature characterization since this had a cycle of 2 hours, the rest of the characterization was done in a single hour. This shows that the approach is viable to optimize the PID once changes to the setup is made, however, it also shows that the current system cannot be optimized further. The solution to this is either to increase insulation or implement a different stabilization algorithm.

9.1 Future work

The results for the 3 qubit GHZ state was successful in showing entanglement and a high quantum algorithm fidelity. However, there are still a lot of future work to be done on the experiment.

The first major improvement would be to switch the current sample for a new one. Making sure the new waveguide is manufactured along the correct axis would put the cycling transition along the direct transition which would increase the detuning between the two direct transitions from $10Ghz$ to $30GHz$. Combining this with a slightly narrower bandwidth for the volume Bragg grating would increase the fidelity a lot. This could allow for generating 4 qubit states which would also allow for more complicated quantum algorithm implementations. The limiting factor at this point would probably be the efficiency.

Other future projects will also be to create one sided waveguides and making active switching work for the interferometer. The one sided waveguides would double the collection efficiency for the photons. The active switching would allow for feed forward operations during quantum algorithms and it would double the rate for every photonic qubit because the qubits could be measured in the correct basis 100% of the time instead of 50%.

Once a stable generation protocol for longer linear cluster states has been implemented with good enough rate more advanced quantum algorithms could be implemented. This includes the 4 qubit Deutsch's algorithm which would be an example of an algorithm that could not be implemented with a product state.

More work is also needed to optimize the temperature control which could be a new PID design or better insulation.

References

[1] Martin Hayhurst Appel. "A Quantum Dot Source of Time-Bin Multi-Photon Entanglement". PhD thesis. University of Copenhagen, July 2021.

[2] M. Arcari et al. "Near-Unity Coupling Efficiency of a Quantum Emitter to a Photonic Crystal Waveguide". In: *Phys. Rev. Lett.* 113 (9 Aug. 2014), p. 093603. DOI: 10.1103/PhysRevLett.113.093603. URL: https://link.aps.org/doi/10.1103/PhysRevLett.113.093603.

[3] HG Barros et al. "Deterministic single-photon source from a single ion". In: *New Journal of Physics* 11.10 (2009), p. 103004.

[4] P. Benioff. "The computer as a physical system: A microscopic quantum mechanical Hamiltonian model of computers as represented by Turing machines". In: *Journal of statistical physics* 22.5 (May 1979). DOI: https://doi.org/10.1007/BF01011339. URL: https://doi.org/10.1007/BF01011339.

[5] Mohamed Benyoucef and Anna Musiał. "Telecom Wavelengths InP-Based Quantum Dots for Quantum Communication". In: *Photonic Quantum Technologies: Science and Applications* 2 (2023), pp. 463–507.

[6] Johannes Borregaard, Anders Søndberg Sørensen and Peter Lodahl. "Quantum networks with deterministic spin–photon interfaces". In: *Advanced Quantum Technologies* 2.5-6 (2019), p. 1800091.

[7] Xin Cao, Michael Zopf and Fei Ding. "Telecom wavelength single photon sources". In: *Journal of Semiconductors* 40.7 (2019), p. 071901.

[8] C Carmesin et al. "Structural and optical properties of InAs/(In) GaAs/GaAs quantum dots with single-photon emission in the telecom C-band up to 77 K". In: *Physical Review B* 98.12 (2018), p. 125407.

[9] Xing Chen et al. "Single photon randomness based on a defect center in diamond". In: *Scientific reports* 9.1 (2019), p. 18474.

[10] Yao Chen et al. "Fiber coupled high count-rate single-photon generated from InAs quantum dots". In: *Journal of Semiconductors* 42.7 (2021), p. 072901.

[11] Beatrice Da Lio et al. "A Pure and Indistinguishable Single-Photon Source at Telecommunication Wavelength". In: *Advanced Quantum Technologies* 5.5 (2022), p. 2200006.

[12] David Deutsch. "Quantum theory, the Church–Turing principle and the universal quantum computer". In: *Proceedings of the Royal Society of London. A. Mathematical and Physical Sciences* 400.1818 (1985), pp. 97–117.

[13] Michel H Devoret, Andreas Wallraff and John M Martinis. "Superconducting qubits: A short review". In: *arXiv preprint cond-mat/0411174* (2004).

[14] Richard P Feynman. "Quantum mechanical computers." In: *Found. Phys.* 16.6 (1986), pp. 507–532.

[15] Christopher C. Gerry and Peter L. Knight. *Introductory Quantum Optics*. New York: Cambridge University Press, 2005.

[16] Yu-Ming He et al. "On-demand semiconductor single-photon source with near-unity indistinguishability". In: *Nature nanotechnology* 8.3 (2013), pp. 213–217.

[17] Xiaoying Huang et al. "Wafer-scale epitaxial low density InAs/GaAs quantum dot for single photon emitter in three-inch substrate". In: *Nanomaterials* 11.4 (2021), p. 930.

[18] Sacha Kocsis et al. “Heralded noiseless amplification of a photon polarization qubit”. In: *Nature Physics* 9.1 (2013), pp. 23–28.

[19] Pieter Kok et al. “Linear optical quantum computing with photonic qubits”. In: *Reviews of modern physics* 79.1 (2007), p. 135.

[20] Peter Kratzer et al. “Shape transition during epitaxial growth of InAs quantum dots on GaAs (001): Theory and experiment”. In: *Physical Review B* 73.20 (2006), p. 205347.

[21] Andreas V. Kuhlmann et al. “Charge noise and spin noise in a semiconductor quantum device”. In: *Nature Physics* 9.9 (July 2013), pp. 570–575. DOI: 10.1038/nphys2688. URL: https://doi.org/10.1038%2Fnphys2688.

[22] Matthias C. Löbl et al. “Excitons in InGaAs quantum dots without electron wetting layer states”. In: *Communications Physics* 2.1 (Aug. 2019). DOI: 10.1038/s42005-019-0194-9. URL: https://doi.org/10.1038%2Fs42005-019-0194-9.

[23] Peter Lodahl, Sahand Mahmoodian and Søren Stobbe. “Interfacing single photons and single quantum dots with photonic nanostructures”. In: *Rev. Mod. Phys.* 87 (2 May 2015), pp. 347–400. DOI: 10.1103/RevModPhys.87.347. URL: https://link.aps.org/doi/10.1103/RevModPhys.87.347.

[24] J McKeever et al. “Deterministic generation of single photons from one atom trapped in a cavity”. In: *Science* 303.5666 (2004), pp. 1992–1994.

[25] T Miyazawa et al. “Single-photon emission at 1.5 μ m from an InAs/InP quantum dot with highly suppressed multi-photon emission probabilities”. In: *Applied Physics Letters* 109.13 (2016), p. 132106.

[26] A. Montanaro. “Quantum algorithms: an overview”. In: *npj Quantum Inf* 2 (Jan. 2016), p. 15023. DOI: https://doi.org/10.1038/npjqi.2015.23. URL: https://doi.org/10.1038/npjqi.2015.23.

[27] P Sreekumari Nair, Karolina P Fritz and Gregory D Scholes. “Evolutionary Shape Control During Colloidal Quantum-Dot Growth”. In: *Small* 3.3 (2007), pp. 481–487.

[28] Roee Ozeri. “The trapped-ion qubit tool box”. In: *Contemporary Physics* 52.6 (2011), pp. 531–550.

[29] Matthias Paul et al. “Single-photon emission at 1.55 μ m from MOVPE-grown InAs quantum dots on InGaAs/GaAs metamorphic buffers”. In: *Applied Physics Letters* 111.3 (2017), p. 033102.

[30] TB Pittman, BC Jacobs and JD Franson. “Demonstration of nondeterministic quantum logic operations using linear optical elements”. In: *Physical Review Letters* 88.25 (2002), p. 257902.

[31] Jarryd J Pla et al. “A single-atom electron spin qubit in silicon”. In: *Nature* 489.7417 (2012), pp. 541–545.

[32] YLA Rezus et al. “Single-photon spectroscopy of a single molecule”. In: *Physical review letters* 108.9 (2012), p. 093601.

[33] Peter W Shor. “Polynomial-time algorithms for prime factorization and discrete logarithms on a quantum computer”. In: *SIAM review* 41.2 (1999), pp. 303–332.

[34] P. Tighineanu et al. “Phonon Decoherence of Quantum Dots in Photonic Structures: Broadening of the Zero-Phonon Line and the Role of Dimensionality”. In: *Phys. Rev. Lett.* 120 (25 June 2018), p. 257401. DOI: 10.1103/PhysRevLett.120.257401. URL: https://link.aps.org/doi/10.1103/PhysRevLett.120.257401.

[35] Konstantin Tiurev and Anders S. Sørensen. “Fidelity measurement of a multiqubit cluster state with minimal effort”. In: *Phys. Rev. Res.* 4 (3 Aug. 2022), p. 033162. DOI: 10.1103/PhysRevResearch.4.033162. URL: https://link.aps.org/doi/10.1103/PhysRevResearch.4.033162.

[36] Ravitej Uppu et al. “Quantum-dot-based deterministic photon–emitter interfaces for scalable photonic quantum technology”. In: *Nature nanotechnology* 16.12 (2021), pp. 1308–1317.

[37] Zhiming M Wang. *Self-assembled quantum dots*. Vol. 1. Springer Science & Business Media, 2007.

[38] Richard J. Warburton. “Single spins in self-assembled quantum dots”. In: *Nature materials* 12.6 (2013), pp. 483–493. DOI: 10.1038/NMAT3585.